Journal of Computational Physics 228 (2009) 5539–5573

Contents lists available at ScienceDirect

Journal of Computational Physics

journal homepage: www.elsevier.com/locate/jcp

Conservative numerical simulation of multi-component transport in two-dimensional unsteady shallow water flow

J. Murillo [a], P. García-Navarro [a,*], J. Burguete [b]

[a] Fluid Mechanics, C.P.S. University of Zaragoza, Maria de Luna 3, 50018 Zaragoza, Spain
[b] Suelo y Agua, Estación Experimental de Aula Dei, CSIC, Zaragoza, Spain

ARTICLE INFO

Article history:
Received 10 November 2008
Received in revised form 20 April 2009
Accepted 27 April 2009
Available online 7 May 2009

MSC:
35L65
65M06
65M12
76M12
76M20

Keywords:
Multi-component transport
Well-balanced approach
Solute constraints
Variable domain
Reactive source terms
Coupled system
Shallow flow
Turbulence
$\kappa-\epsilon$ model

ABSTRACT

An explicit finite volume model to simulate two-dimensional shallow water flow with multi-component transport is presented. The governing system of coupled conservation laws demands numerical techniques to avoid unrealistic values of the transported scalars that cannot be avoided by decreasing the size of the time step. The presence of non conservative products such as bed slope and friction terms, and other source terms like diffusion and reaction, can make necessary the reduction of the time step given by the Courant number. A suitable flux difference redistribution that prevents instability and ensures conservation at all times is used to deal with the non-conservative terms and becomes necessary in cases of transient boundaries over dry bed. The resulting method belongs to the category of well-balanced Roe schemes and is able to handle steady cases with flow in motion. Test cases with exact solution, including transient boundaries, bed slope, friction, and reaction terms are used to validate the numerical scheme. Laboratory experiments are used to validate the techniques when dealing with complex systems as the $\kappa-\epsilon$ model. The results of the proposed numerical schemes are compared with the ones obtained when using uncoupled formulations.

1. Introduction

There is a significant interest in the description of the transport of dissolved chemical species into natural waters caused by the discharge of agricultural, industrial and domestic effluents but also of the transport of nutrients involved in biological processes. Also, it is of primary importance the interaction with the soil, as the possible transfer of chemical agents between surface water and soil can cause potential threat to the quality of the environment. These processes are not only susceptible to continuous variations in the incorporation of chemical agents in time, they also depend on the variation of the transference area in flooding events, where it is also of importance the recession part where the dissolved chemicals stored in ponds can affect the biological quality of the inundation areas or indirectly reach groundwaters.

* Corresponding author. Tel.: +34 976761881; fax: +34 976761882.
E-mail address: pigar@unizar.es (P. García-Navarro).

0021-9991/$ - see front matter © 2009 Elsevier Inc. All rights reserved.
doi:10.1016/j.jcp.2009.04.039

When evaluating real flows in rivers the cost of the non-simplified three-dimensional numerical methods can be avoided using depth integrated models, as water in rivers and estuaries are usually well-mixed and flows are pressure-driven, so the dissolved chemicals are generally distributed uniformly over a water column.

The development of robust and efficient explicit finite volume models of shallow water flow has been the matter of recent research in the computational hydraulics literature. A few efforts have been reported on the search for the best methods able to preserve the exact conservation property (C-property) [29] in presence of flow over irregular geometries [4,17]. Understanding that other processes, like that of pollutant transport, are determined by the characteristics of the fluid flow, the shallow water model has been accepted as the basis for the development of more ambitious environmental or hydraulic models. For many applications, the standard advection–diffusion equation has been used to model the dynamics of a transported scalar together with the shallow water equations for the hydrodynamic variables [24]. Extensions of the numerical models to ensure the correct resolution of the enlarged system of equations have followed different approaches. Several authors [2,7,10] report on the use of the uncoupled system of equations whereas others [3,6,15] consider the convenience of solving the shallow water and the transport equations in coupled form to deal with steady and unsteady flow even in presence of discontinuities of both solute concentration and water depth. Considering that the conserved quantity is the solute volume and not the solute concentration, the coupled formulation of the system and the use of an extended Jacobian matrix to develop the flux difference splitting is not always a sufficient condition in complex cases, as demonstrated in [16], in order to ensure conservation and the required positivity in the concentrations.

When dealing with simulation problems that involve bed variations and transient flow over a dry bed, these flow features impose a heavier restriction than the classical Courant–Friedrichs–Lewy (CFL) condition [8,14,28] on the time step size that may lead to inefficient computations. It is possible to avoid the necessity of reducing the time step and, at the same time, to prevent instability and to ensure conservation at all times by a suitable flux difference redistribution [17].

When moving to more complex applications that require the transport and reaction of diverse scalar magnitudes (mass concentration, energy, etc.) in complex geometries, the numerical schemes must be carefully formulated to ensure at the same time conservation, stability and accuracy of the results. For that reason, an effort can be made to extend the method based on the coupled formulation, the control on the positivity of the scalars transported and the redistribution of the fluxes that recovers the maximum time step for multivariable transport. The interest in modelling biological processes in new storage areas with dissolved chemicals and nutrients, during and after flooding events, with not extremely time consuming effort, justify this analysis.

This work will present a formulation of the governing equations of a general 2D shallow water flow with multivariable transport involving diffusion and reaction. Then, first and second order finite volume schemes, already tested in simpler simulations [15,18], will be outlined and extended for the simulation of the defined system of equations. Extension to second order on triangular grids can be formulated for instance by means of the MUSCL-Hancock scheme [2,27]. The gradient slope limitation used in this work in combination with the MUSCL-Hancock scheme has been used in order to follow previous numerical works dealing with second order limitation on triangular unstructured grids. Flux or slope limiting functions defined in one-dimensional problems in order to ensure the TVD property on numerical solutions do not ensure this property in two-dimensional problems except in certain trivial cases [12]. Positively conservative schemes specially designed for unstructured grids have been widely reported [1,31].

The emphasis will be put on the necessity to perform a systematic control over the positivity of the concentrations of the transported components always additional to the required C-property. Furthermore, a conservative flux redistribution, previously proposed for shallow water flows with a single component [17], to avoid excessive time step reduction will be generalized to the more complex situation. As a first application, the modelling of the purely advective transport of three mutually independent components in a two-dimensional unsteady flow over dry bed will be presented and compared to the analytical solution. Then, the simulation of a two-component system with reaction terms is considered. Examples with analytical solution have been selected in order to emphasize the main features of the numerical solution achieved with different techniques. The reaction term is considered as a new source term.

The depth average $\kappa-\epsilon$ model, widely used in environmental applications, has been used as an example of more sophisticated formulations in which the transported variables affect the flow evolution. Two laboratory test cases with experimental data have been selected in order to validate the numerical approaches.

2. Governing equations

The solute transport and water flow under shallow conditions can be formulated by means of the depth averaged set of equations expressing water volume conservation, solute volume conservation and water momentum conservation. That system of partial differential equations will be formulated here in coupled form as follows:

$$\frac{\partial \mathbf{U}}{\partial t}+\frac{\partial \mathbf{F}(\mathbf{U})}{\partial x}+\frac{\partial \mathbf{G}(\mathbf{U})}{\partial y}=\mathbf{S}(\mathbf{U})+\mathbf{R}(\mathbf{U})+\vec{\nabla}\mathbf{D}(\mathbf{U}) \tag{1}$$

where

$$\mathbf{U}=(\,h \quad q_x \quad q_y \quad h\phi_1 \quad h\phi_2 \quad \cdots \quad h\phi_p\,)^T \tag{2}$$

are the conserved variables with h representing the water depth, $q_x = hu$ and $q_y = hv$, with (u, v) the depth averaged components of the velocity vector $\mathbf{u}$ along the x and y coordinates, respectively, and $\phi_1, \phi_2, \ldots, \phi_p$ represent the scalar depth averaged concentration of the different quantities transported. The fluxes of these variables are given by:

$$\begin{aligned}\mathbf{F} &= \begin{pmatrix} q_x & \frac{q_x^2}{h} + \frac{1}{2}gh^2 & \frac{q_x q_y}{h} & q_x\phi_1 & q_x\phi_2 & \cdots & q_x\phi_p \end{pmatrix}^T \\ \mathbf{G} &= \begin{pmatrix} q_y & \frac{q_x q_y}{h} & \frac{q_y^2}{h} + \frac{1}{2}gh^2 & q_y\phi_1 & q_y\phi_2 & \cdots & q_y\phi_p \end{pmatrix}^T \end{aligned} \tag{3}$$

where g is the acceleration of the gravity. The source terms of the system are split in three kinds of terms. The bed slope and friction source terms of the momentum equations:

$$\mathbf{S} = \begin{pmatrix} 0 & gh(S_{ox} - S_{fx}) & gh(S_{oy} - S_{fy}) & 0 & 0 & \cdots & 0 \end{pmatrix}^T \tag{4}$$

where the bed slopes of the bottom level z are

$$S_{ox} = -\frac{\partial z}{\partial x}, \quad S_{oy} = -\frac{\partial z}{\partial y} \tag{5}$$

and the friction losses are written in terms of the Manning's roughness coefficient n:

$$S_{fx} = \frac{n^2 u\sqrt{u^2 + v^2}}{h^{4/3}}, \quad S_{fy} = \frac{n^2 v\sqrt{u^2 + v^2}}{h^{4/3}} \tag{6}$$

We will assume that the reaction source terms $\mathbf{R}$ will be defined by every particular application.

The diffusion terms are based on the following formulation:

$$\mathbf{D} = \begin{pmatrix} 0 & \mathbf{K}_u h\vec{\nabla}u & \mathbf{K}_v h\vec{\nabla}v & \mathbf{K}_1 h\vec{\nabla}\phi_1 & \mathbf{K}_2 h\vec{\nabla}\phi_2 & \cdots & \mathbf{K}_p h\vec{\nabla}\phi_p \end{pmatrix}^T \tag{7}$$

where each $\mathbf{K}$ is an empirical dispersion matrix. The particular form of the matrix elements will be detailed in the applications section.

System (1) is time dependent, non linear, and contains advection, diffusion, reaction and source terms. Under the hypothesis of dominant advection it can be classified and numerically dealt with as belonging to the family of hyperbolic systems. The mathematical properties of (1) include the existence of a Jacobian matrix, $\mathbf{J_n}$, of the normal flux $\mathbf{En}$, with $\mathbf{En} = \mathbf{F}n_x + \mathbf{G}n_y$, defined as

$$\mathbf{J_n} = \frac{\partial \mathbf{En}}{\partial \mathbf{U}} = \frac{\partial \mathbf{F}}{\partial \mathbf{U}}n_x + \frac{\partial \mathbf{G}}{\partial \mathbf{U}}n_y \tag{8}$$

This Jacobian can be used to form the basis of the upwind numerical discretization that will be outlined in next section.

3. Finite volume model

To introduce the finite volume scheme, (1) is integrated in a volume or grid cell Ω:

$$\frac{\partial}{\partial t}\int_\Omega \mathbf{U}\,d\Omega + \int_\Omega (\vec{\nabla}\mathbf{E})\,d\Omega = \int_\Omega \mathbf{S}\,d\Omega + \int_\Omega \mathbf{R}\,d\Omega + \int_\Omega (\vec{\nabla}\mathbf{D})\,d\Omega \tag{9}$$

Following previous work, it is assumed that the third integral can be reformulated as [30]

$$\int_\Omega \mathbf{S}\,d\Omega = \oint_{\partial\Omega} (\mathbf{Tn})\,dl \tag{10}$$

where $\mathbf{T}$ is a suitable numerical source matrix. This enables the following formulation

$$\frac{\partial}{\partial t}\int_\Omega \mathbf{U}\,d\Omega + \oint_{\partial\Omega} \mathbf{En}\,dl = \oint_{\partial\Omega} \mathbf{Tn}\,dl + \oint_{\partial\Omega} (\mathbf{Dn})\,dl + \int_\Omega \mathbf{R}\,d\Omega \tag{11}$$

When the domain is sub-divided in cells Ω_i (see Fig. 1), using a mesh fixed in time, (11) can also be applied to each cell:

$$\frac{\partial}{\partial t}\int_\Omega \mathbf{U}_i\,d\Omega_i + \sum_{k=1}^{NE}\int_{e_k}^{e_{k+1}} \mathbf{E}_j\mathbf{n}_k\,dl_k = \sum_{k=1}^{NE}\int_{e_k}^{e_{k+1}} \mathbf{T}_k\mathbf{n}_k\,dl_k + \sum_{k=1}^{NE}\int_{e_k}^{e_{k+1}} \mathbf{D}_k\mathbf{n}_k\,dl_k + \int_\Omega \mathbf{R}\,d\Omega \tag{12}$$

where $\mathbf{n}_k = (n_x, n_y)$, is the outward unit normal vector to the cell edge k, j is a neigbouring cell of i connected through the edge k, $\mathbf{E}_j$ is the function $\mathbf{E}$ at the neighbour cell j, l_k is the corresponding edge length, NE is the number of edges in the cell and $\mathbf{T}_k$ and $\mathbf{D}_k$ to be defined. Eq. (12) can be written as

$$\frac{\partial}{\partial t}\int_\Omega \mathbf{U}_i\,d\Omega_i + \sum_{k=1}^{NE}\int_{e_k}^{e_{k+1}} \delta\mathbf{E}_k\mathbf{n}_k\,dl_k + \sum_{k=1}^{NE}\int_{e_k}^{e_{k+1}} \mathbf{E}_i\mathbf{n}_k\,dl_k = \sum_{k=1}^{NE}\int_{e_k}^{e_{k+1}} \mathbf{T}_k\mathbf{n}_k\,dl_k + \sum_{k=1}^{NE}\int_{e_k}^{e_{k+1}} \mathbf{D}_k\mathbf{n}_k\,dl_k + \int_\Omega \mathbf{R}\,d\Omega \tag{13}$$

where $\delta\mathbf{E}_k = \mathbf{E}_j - \mathbf{E}_i$, with $\mathbf{E}_j$ and $\mathbf{E}_i$ the function $\mathbf{E}$ at cells j and i, respectively.

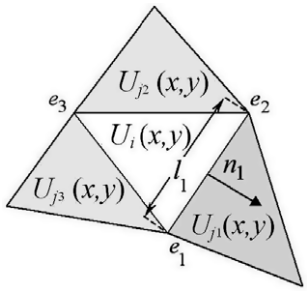

Fig. 1. Cell parameters.

3.1. First order scheme

In first order the vector quantities are uniform per cell (Fig. 2). Using this together with the following geometric relationship

$$\sum_{k=1}^{NE} \mathbf{n}_k l_k = 0 \tag{14}$$

and approaching the reaction term as

$$\int_{\Omega} \mathbf{R}\, d\Omega = \mathbf{R}_i A_i \tag{15}$$

with uniform values for $\mathbf{T}_k$ and $\mathbf{D}_k$ in each edge, (11) reduces to

$$\frac{(\mathbf{U}_i^{n+1} - \mathbf{U}_i^n)}{\Delta t} A_i + \sum_{k=1}^{NE} (\delta \mathbf{E} - \mathbf{T})_k \mathbf{n}_k l_k = \sum_{k=1}^{NE} \mathbf{D}_k \mathbf{n}_k l_k + \mathbf{R}_i A_i \tag{16}$$

with A_i the area of cell Ω_i.

Due to the non-linear character of the flux $\mathbf{E}$, the definition of an approximated Jacobian matrix, $\widetilde{\mathbf{J}}_{\mathbf{n},k}$, allows for a local Roe type linearization and is exploited here [22]. This approach provides a set of $3 + p$ real eigenvalues $\tilde{\lambda}_k^m$ and eigenvectors $\tilde{\mathbf{e}}_k^m$, constructed with the following averaged variables

$$\begin{aligned} &\tilde{u}_k = \frac{u_i\sqrt{h_i} + u_j\sqrt{h_j}}{\sqrt{h_i} + \sqrt{h_j}}, \quad \tilde{v}_k = \frac{v_i\sqrt{h_i} + v_j\sqrt{h_j}}{\sqrt{h_i} + \sqrt{h_j}}, \quad \tilde{c}_k = \sqrt{g\frac{h_i + h_j}{2}} \\ &\tilde{\phi}_1 = \frac{\phi_{1,j}\sqrt{h_i} + \phi_{1,i}\sqrt{h_j}}{\sqrt{h_i} + \sqrt{h_j}}, \quad \ldots, \quad \tilde{\phi}_p = \frac{\phi_{p,j}\sqrt{h_i} + \phi_{p,i}\sqrt{h_j}}{\sqrt{h_i} + \sqrt{h_j}} \end{aligned} \tag{17}$$

leading to

$$\begin{aligned} &\tilde{\lambda}_k^1 = (\tilde{\mathbf{u}}\mathbf{n} + \tilde{c})_k, \quad \tilde{\lambda}_k^2 = (\tilde{\mathbf{u}}\mathbf{n})_k, \quad \tilde{\lambda}_k^3 = (\tilde{\mathbf{u}}\mathbf{n} - \tilde{c})_k \\ &\tilde{\lambda}_k^4 = \tilde{\lambda}_k^5 = \cdots = \tilde{\lambda}_k^{3+p} = (\tilde{\mathbf{u}}\mathbf{n})_k \end{aligned} \tag{18}$$

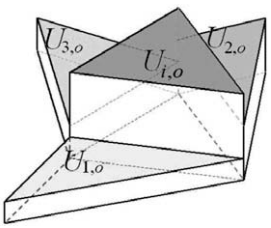

Fig. 2. Piecewise constant representation of the variable U.

and

$$\tilde{\mathbf{e}}_k^1 = \begin{pmatrix} 1 \\ \tilde{u} + \tilde{c}n_x \\ \tilde{v} + \tilde{c}n_y \\ \tilde{\phi}_1 \\ \tilde{\phi}_2 \\ \cdots \\ \tilde{\phi}_p \end{pmatrix}_k, \quad \tilde{\mathbf{e}}_k^2 = \begin{pmatrix} 1 \\ -\tilde{c}n_y \\ -\tilde{c}n_x \\ 0 \\ 0 \\ \cdots \\ 0 \end{pmatrix}_k, \quad \tilde{\mathbf{e}}_k^3 = \begin{pmatrix} 1 \\ \tilde{u} - \tilde{c}n_x \\ \tilde{v} - \tilde{c}n_y \\ \widetilde{\phi_1} \\ \widetilde{\phi_2} \\ \cdots \\ \tilde{\phi}_p \end{pmatrix}_k$$
$$\tilde{\mathbf{e}}_k^4 = \begin{pmatrix} 0 \\ 0 \\ 0 \\ 1 \\ 0 \\ \cdots \\ 0 \end{pmatrix}_k, \quad \tilde{\mathbf{e}}_k^5 = \begin{pmatrix} 0 \\ 0 \\ 0 \\ 0 \\ 1 \\ \cdots \\ 0 \end{pmatrix}_k, \quad \ldots, \quad \tilde{\mathbf{e}}_k^{3+p} = \begin{pmatrix} 0 \\ 0 \\ 0 \\ 0 \\ 0 \\ \cdots \\ 1 \end{pmatrix}_k \tag{19}$$

Matrices $\widetilde{\mathbf{P}}_k$, and $\widetilde{\mathbf{P}}_k^{-1}$, can be built using the eigenvectors $\tilde{\mathbf{e}}_k^m$ of $\widetilde{\mathbf{J}}_{\mathbf{n},k}$ so that they diagonalize it

$$\widetilde{\mathbf{J}}_{\mathbf{n},k} = (\widetilde{\mathbf{P}}\widetilde{\mathbf{\Lambda}}\widetilde{\mathbf{P}}^{-1})_k, \quad \widetilde{\mathbf{P}}_k = \begin{pmatrix} \tilde{\mathbf{e}}_k^1 & \tilde{\mathbf{e}}_k^2 & \tilde{\mathbf{e}}_k^3 & \tilde{\mathbf{e}}_k^4 & \tilde{\mathbf{e}}_k^5 & \cdots & \tilde{\mathbf{e}}_k^{3+p} \end{pmatrix} \tag{20}$$

where $\widetilde{\mathbf{\Lambda}}$ is the diagonal eigenvalues $\tilde{\lambda}_k^m$ matrix. Also, from the approximate Jacobian [22]

$$\widetilde{\mathbf{J}}_{\mathbf{n},k}\tilde{\mathbf{e}}_k^m = \tilde{\lambda}_k^m \tilde{\mathbf{e}}_k^m, \quad m = 1, 2, 3, \ldots, 3+p \tag{21}$$

The problem can be reduced to a one-dimensional Riemann problem projected onto the direction $\mathbf{n}$ at each cell edge [11]. Following a flux difference procedure, the difference in vector $\mathbf{U}$ across the grid edge is projected onto the matrix eigenvectors basis

$$\delta\mathbf{U}_k = \sum_{m=1}^{3+p} (\alpha\tilde{\mathbf{e}})_k^m \tag{22}$$

where the expression of coefficients α_k are:

$$\begin{aligned} &\alpha_k^{1,3} = \frac{\delta h_k}{2} \pm \frac{1}{2\tilde{c}_k}(\delta\mathbf{q}_k - \tilde{\mathbf{u}}_k\delta h_k)\mathbf{n}_k, \quad \alpha_k^2 = \frac{1}{\tilde{c}_k}(\delta\mathbf{q}_k - \tilde{\mathbf{u}}_k\delta h_k)\mathbf{n}_{T,k} \\ &\alpha_k^4 = \delta(h\phi_1)_k - (\tilde{\phi}_1\delta h)_k \\ &\alpha_k^5 = \delta(h\phi_2)_k - (\tilde{\phi}_2\delta h)_k, \quad \ldots, \quad \alpha_k^{3+p} = \delta(h\phi_p)_k - (\tilde{\phi}_p\delta h)_k \end{aligned} \tag{23}$$

with $\mathbf{n}_{T,k} = (-n_y, n_x)$. The $\delta(\mathbf{En})_k$ contributions at a cell edge k can be written as:

$$\delta(\mathbf{En})_k = \sum_{m=1}^{3+p} (\tilde{\lambda}\alpha\tilde{\mathbf{e}})_k^m \tag{24}$$

Following the unified discretization in [5] the non-conservative term $(\mathbf{Tn})_k$ at a cell edge is written

$$(\mathbf{Tn})_k = \begin{pmatrix} 0 & -g\tilde{h}(\delta z + d_{\mathbf{n}}S_f)n_x & -g\tilde{h}(\delta z + d_{\mathbf{n}}S_f)n_y & 0 & 0 & \cdots & 0 \end{pmatrix}_k^T \tag{25}$$

with the discretization of the friction term based on [19]

$$S_{f,k} = \left(\frac{n^2 \tilde{\mathbf{u}}\mathbf{n}|\tilde{\mathbf{u}}|d_{\mathbf{n}}}{\max(h_i, h_j)^{4/3}} \right)_k \tag{26}$$

where $d_{\mathbf{n}}$ is the distance between cell centroids sharing edge k projected onto the $\mathbf{n}$ direction as displayed in Fig. 3.

Both the bed slope and the friction term can be split onto the basis of eigenvectors in order to enforce the discrete equilibrium with the flux derivative terms (24), so (C-property) is ensured in steady cases with nil and not nil velocity [19,23]:

$$(\mathbf{Tn})_k = \widetilde{\mathbf{P}}_k\mathbf{B}_k = \sum_{m=1}^{3+p} (\beta^m\tilde{\mathbf{e}}^m)_k \tag{27}$$

with $\mathbf{B}_k = (\,\beta_1 \quad \beta_2 \quad \beta_3 \quad \beta_4 \quad \beta_5 \quad \cdots \quad \beta_{3+p}\,)_k^T$. The coefficients are

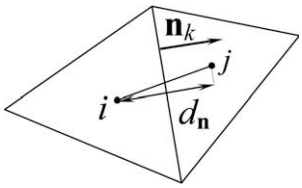

Fig. 3. Normal distance $d_{\mathbf{n}}$ between two cells.

$$\begin{aligned} &\beta_k^{1,3} = \mp\frac{\tilde{c}_k}{2}(\delta z + d_{\mathbf{n}} S_f)_k, \quad \beta_k^2 = 0 \\ &\beta_k^4 = \beta_k^5 = \cdots = \beta_k^{3+p} = 0 \end{aligned} \tag{28}$$

The explicit first order upwind scheme for the non-diffusive and non-reacting part of (16) gets the form:

$$\mathbf{U}_i^* = \mathbf{U}_i^n + \Delta t \sum_{k=1}^{NE} \mathbf{\Psi}_{i,k}^n \tag{29}$$

expressed as sum of each edge contribution, $\mathbf{\Psi}_{i,k}$

$$\mathbf{\Psi}_{i,k} = \sum_{m=1}^{3+p} ((\tilde{\lambda}^- \alpha - \beta^-)\tilde{\mathbf{e}})_k^m l_k / A_i \tag{30}$$

where $\tilde{\lambda}^- = \frac{1}{2}(\tilde{\lambda} - |\tilde{\lambda}|)$ and $\beta^- = \frac{1}{2}(1 - sign(\tilde{\lambda}))\beta$. The value in (29) provides a predicted value of the solution of the non-diffusive and non-reacting system, and then, the reaction terms can be simply added using a first order approach

$$\mathbf{U}_i^{**} = \mathbf{U}_i^* + \Delta t \mathbf{R}_i^* \tag{31}$$

with $\mathbf{R}_i^* = \mathbf{R}(\mathbf{U}_i^*) = (0 \quad 0 \quad 0 \quad R_1^* \quad R_2^* \quad \cdots \quad R_p^*)_i^T$, that can be evaluated explicitly

$$R_s^* = \begin{cases} \min\{R_s^*, U_{3+s}^* \Delta t^{-1}\} & \text{if } R_s^* < 0 \\ R_s^* & \text{if } R_s^* > 0 \end{cases} \tag{32}$$

for $s = 1, \ldots, p$. Otherwise, it can be evaluated implicitly only in the case $R_s^* < 0$

$$U_{3+s}^{**} = U_{3+s}^* \left(1 - \frac{R_s^* \Delta t}{U_{3+s}^*}\right)^{-1} \tag{33}$$

Finally the solution including also the diffusive terms is

$$\mathbf{U}_i^{n+1} = \mathbf{U}_i^{**} + \Delta t \mathbf{D}_i^{n+1} \tag{34}$$

The final value including diffusion is computed by means of an implicit method over the diffusion term in a second step [15]. The numerical diffusion step becomes unconditionally stable, as the resolution matrix is positive defined.

3.2. Second order scheme

The spatial discrete representation of the functions can be improved using information of the neighbour cells. The reconstruction functions can be defined as piecewise linear representations in the cells so that the scheme becomes a second order in space approximation [13]. As the cell representation function must be unique to preserve conservation, the techniques described in this section can only be applied to triangular cells because the number of edges in which stability conditions are required cannot exceed the number of points used to define the representation function itself [11].

The piecewise linear reconstruction of a scalar variable U, over an element i with centroid at (x_o, y_o) is expressed as

$$U_i(x, y) = U_{i,o} + \mathbf{r}(x, y)\mathbf{L}_{U,i} \tag{35}$$

where $\mathbf{r}$ is the position vector from the centroid, and $\mathbf{L}$ is the cell slope. Using (14) the advective part of (13) can be formulated as:

$$\sum_{k=1}^{NE} (\delta \mathbf{E})_{JI,k} \mathbf{n}_k l_k + \sum_{k=1}^{NE} (\delta \mathbf{E})_{Ii,k} \mathbf{n}_k l_k \tag{36}$$

while the non-conservative product in (13) is formulated as:

$$\sum_{k=1}^{NE} (\mathbf{T})_{JI,k} \mathbf{n}_k l_k + \sum_{k=1}^{NE} (\mathbf{T})_{Ii,k} \mathbf{n}_k l_k \tag{37}$$

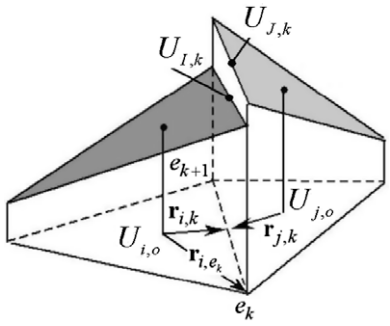

Fig. 4. Linear representation by cells.

with $\delta\mathbf{E}_{JI,k} = \mathbf{E}_{J,k} - \mathbf{E}_{I,k}$, where $\mathbf{E}_{J,k}$ and $\mathbf{E}_{I,k}$ are computed evaluating the conserved variables $\mathbf{U}$ at the corresponding middle-edge position and plane (Fig. 4), $\delta\mathbf{E}_{Ii,k} = \mathbf{E}_{I,k} - \mathbf{E}_{i,k}$ and

$$\begin{aligned} &U_{I,k} = U_{i,o} + \mathbf{r}_{i,k}\mathbf{L}_{U,i}, \quad U_{J,k} = U_{j,o} + \mathbf{r}_{j,k}\mathbf{L}_{U,j} \\ &\mathbf{r}_{i,k} = \frac{1}{2}(\mathbf{r}_{i,e_k} + \mathbf{r}_{i,e_{k+1}}), \quad \mathbf{r}_{j,k} = \frac{1}{2}(\mathbf{r}_{j,e_k} + \mathbf{r}_{j,e_{k+1}}) \end{aligned} \tag{38}$$

It must be remarked that the linear reconstruction must be done ensuring

$$U_k^{min} \leqslant U_{J,k} \leqslant U_k^{max}, \quad U_k^{min} \leqslant U_{I,k} \leqslant U_k^{max} \tag{39}$$

where $U_k^{min} = \min(U_{i,o}, U_{j,o})$ and $U_k^{max} = \max(U_{i,o}, U_{j,o})$. Different forms to define the cell slope can be formulated [1,11,17,31].

Then, the second order in space approach can be defined as

$$\frac{(\mathbf{U}_i^* - \mathbf{U}_i^n)}{\Delta t} A_i + \sum_{k=1}^{NE} (\delta\mathbf{E} - \mathbf{T})_{JI,k} \mathbf{n}_k l_k + \sum_{k=1}^{NE} (\delta\mathbf{E} - \mathbf{T})_{Ii,k} \mathbf{n}_k l_k = 0 \tag{40}$$

To be numerically stable, it is necessary to move to second order in time and space, using, for instance, a two-step method (MUSCL-Hancock) [27]:

$$\begin{aligned} &\mathbf{U}_{I,k}^{n+1/2} = \mathbf{U}_i^n + \frac{\Delta t}{2} \sum_{k=1}^{NE} \mathbf{\Psi}_{Ii,k}^n \\ &\mathbf{U}_i^* = \mathbf{U}_i^n + \Delta t \sum_{k=1}^{NE} \mathbf{\Psi}_{JI,k}^{n+1/2} + \Delta t \sum_{k=1}^{NE} \mathbf{\Psi}_{Ii,k}^{n+1/2} \end{aligned} \tag{41}$$

with $\mathbf{\Psi}_{JI,k} = \sum_{m=1}^{3+p} ((\tilde{\lambda}^- \alpha - \beta^-)\tilde{\mathbf{e}})_{JI,k}^m l_k / A_i$ where

$$\begin{aligned} &\beta_{JI,k}^{1,3} = \mp \frac{\tilde{c}_{JI,k}}{2} (\delta z_{JI,k} + d_{\mathbf{n}} S_{JI,k}), \quad \beta_{JI,k}^2 = 0 \\ &\beta_{JI,k}^4 = \beta_{IJI,k}^5 = \cdots = \beta_{JI,k}^{3+p} = 0 \end{aligned} \tag{42}$$

and $\mathbf{\Psi}_{Ii,k} = \sum_{m=1}^{3+p} ((\tilde{\lambda}\alpha - \beta)\tilde{\mathbf{e}})_{Ii,k}^m l_k / A_i$ where

$$\begin{aligned} &\beta_{Ii,k}^{1,3} = \mp \frac{\tilde{c}_{Ii,k}}{2} (\delta z_{Ii,k}), \quad \beta_{Ii,k}^2 = 0 \\ &\beta_{Ii,k}^4 = \beta_{Ii,k}^5 = \cdots = \beta_{Ii,k}^{3+p} = 0 \end{aligned} \tag{43}$$

Special care is necessary when defining the interpolation planes involving the source terms. In this case the adequate interpolation plane for the conserved variable h is the water level surface, $h + z$ [17], ensuring the required C-property in second order approach. The empirical Manning friction formula applied cannot be transformed into a linear space variation over the cell. Then, for simplicity, when second order is imposed the friction term $S_{Ii,k}$ is considered nil. The reactive source terms would be structured as in Eqs. (31)–(33). Also, the diffusive part can be solved in a final step as indicated in Eq. (34).

3.3. Multi-component transport constraints

In the algorithms formulated in Eqs. (29) and (41) for the coupled system the conserved variable in the mass conservation equation of every transported component is $h\phi_s$ so that the final value of solute concentration ϕ_s is computed as a ratio between the conserved solute mass and the water depth. This can lead to unbounded and unrealistic concentration values in some complex cases with important relative water depth variations, with independence of the time step size used. This was

identified in [18] and a conservative redistribution of the solute mass fluxes was presented. The proposal in the present work is to apply the same idea to each transported scalar in the set of equations. For clarity, it is convenient to define the cell edge flux as

$$\boldsymbol{\Psi}_{i,k} = \left(\Psi^{h}_{i,k} \quad \Psi^{hu}_{i,k} \quad \Psi^{hv}_{i,k} \quad \Psi^{h\phi_1}_{i,k} \quad \Psi^{h\phi_2}_{i,k} \quad \cdots \quad \Psi^{h\phi_p}_{i,k} \right)^T \tag{44}$$

The procedure is based in the definition of a virtual solute concentration ϕ_v for each s transported variable at each cell edge between cells i and j for $s = 1, \ldots, p$.

$$\phi_v = \begin{cases} \max\{\phi_{s,i}, \phi_{s,j}\}, & \text{if } \delta\phi^{n+1}_{s,k} < 0 \text{ and } \Psi^{h}_{i,k} < 0 \text{ and } \tilde{\lambda}^{3+s,-}_{i,k} = 0 \\ \min\{\phi_{s,i}, \phi_{s,j}\}, & \text{if } \delta\phi^{n+1}_{s,k} > 0 \text{ and } \Psi^{h}_{i,k} < 0 \text{ and } \tilde{\lambda}^{3+s,-}_{i,k} = 0 \\ \tilde{\phi}_{s,k}, & \text{otherwise} \end{cases} \tag{45}$$

with $\delta\phi^{n}_{s,k} = \phi^{n}_{s,j} - \phi^{n}_{s,i}$, so that, in general, the solute mass flux updating cell i coming from edge k, $\Psi^{h\phi_s}_{i,k}$, and that updating cell j coming from the same edge interface, $\Psi^{h\phi_s}_{j,k}$, are redefined as:

$$\begin{aligned} \Psi^{h\phi_s}_{i,k} &= \phi_v \Psi^{h}_{i,k} \\ \Psi^{h\phi_s}_{j,k} &= \Psi^{h\phi_s}_{j,k} + (\tilde{\phi}_{s,k} - \phi_v)\Psi^{h}_{i,k} r_A \end{aligned} \tag{46}$$

with $r_A = A_i/A_j$, to preserve conservation.

The flux correction in (46) is necessary even if no source terms are present. But when friction and bed slope terms are included another source of numerical oscillations may arise in the case of mixed/clean fronts over irregular domains. To avoid this, again, a conservative redistribution of the flux is proposed. In cases where $\phi^{n}_{s,i} = 0,\ \phi^{n}_{s,j} > 0,\ h^{n}_{i} > 0,\ h^{n}_{j} > 0$ and $\Psi^{h\phi_s}_{i,k} < 0$ the fluxes are redefined as follows:

$$\begin{aligned} \Psi^{h\phi_s}_{j,k} &= \Psi^{h\phi_s}_{j,k} + \Psi^{h\phi_s}_{i,k} r_A \\ \Psi^{h\phi_s}_{i,k} &= 0 \quad \text{when } \phi^{n}_{s,i} = 0,\ \phi^{n}_{s,j} > 0,\ h^{n}_{i} > 0,\ h^{n}_{j} > 0,\ \Psi^{h\phi_s}_{i,k} < 0 \end{aligned} \tag{47}$$

This situation is equivalent to the generation of negative water depths in wetting/drying advance, and is independent of the size of the time step used [17]. When the wetting/drying front contains solute the analysis of the equivalent mixed/clean front is unnecessary as all the variables are nil in one cell. The situation becomes more complicated when mixed/clean fronts move over a completely wet case, because it is possible to find situations where water flux can cross the associated edge but solute mass flux cannot. For that reason the correction in (47) is proposed. As in this case the associated cell edge acts

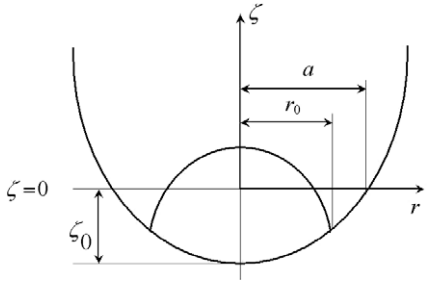

Fig. 5. Initial free surface and water depth profile for the parabolic basin test.

Table 1
Summary of cases for the long wave resonance in a circular parabolic frictionless basin with solute.

Case	Interpolated variable	Flux redistribution	Coupled system	ϕ_1	ϕ_2	ϕ_3
1	No one	Yes	Yes	f_1	f_2	f_3
2	No one	Yes	Yes	f_1	0	0
3	No one	Yes	Yes	0	f_2	0
4	No one	Yes	Yes	0	0	f_3
5	$\phi_1,\ \phi_2,\ \phi_3$	Yes	Yes	f_1	f_2	f_3
6	$q_x,\ q_y,\ \phi_1,\ \phi_2,\ \phi_3$	Yes	Yes	f_1	f_2	f_3
7	No one	No	Yes	f_1	f_2	f_3
8	h	Yes	Yes	0	0	0
9	$h,\ q_x,\ q_y$	Yes	Yes	0	0	0
10	No one	No	No	f_1	f_2	f_3

temporally as a solid wall, in order to ensure conservation in the following time step it is necessary to impose a condition of zero velocity in the normal direction to the cell edge.

If second order is imposed over the conserved variables the final value of the component ϕ_s depends on the interpolation functions used in h and $h\phi_s$ and unrealistic values of solute concentration can appear. The oscillations in the solute concentration can be avoided by reducing locally the scheme to first order but, in presence of strong spatial variations in the water depth, this technique is overly restrictive and leads to a first order solution. When this option is not desirable, extrapolation of the solute concentration ϕ_s, keeping first order over the water depth, is another possibility, providing the most accurate results for the solute concentration [18]. Once the interpolation functions are correctly solved, the cell edge redistributions (46) and (47) are applied to the $\mathbf{\Psi}_{Il,k}$ and $\mathbf{\Psi}_{Ii,k}$ fluxes.

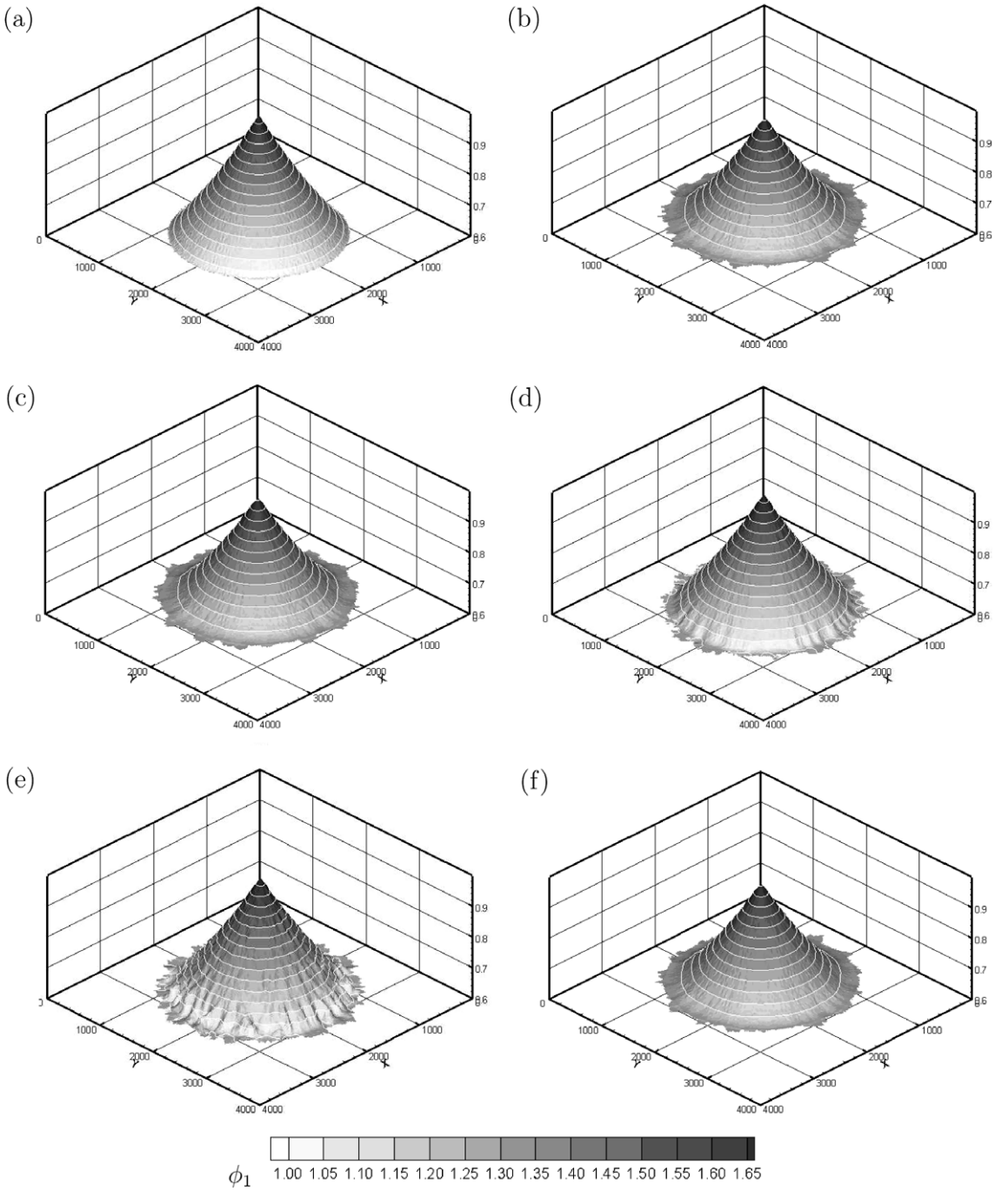

Fig. 6. 3D view of the exact distribution of ϕ_1 at time $4T$ (a), and computed distribution of ϕ_1 at time $4T$ for cases 1, 2 and 5–7 in (b)–(f), respectively.

3.4. Cell conservative flux redistribution

In the previous section numerical techniques to avoid unrealistic cases and numerical oscillations independent of the time step chosen have been presented. On the other hand, it has been previously reported that the presence of source terms reduces the time step size compatible with numerical stability of explicit schemes under certain conditions as compared to the homogeneous case. The CFL stability condition for an explicit scheme applied to solve a homogeneous conservation law is governed by the grid size and the eigenvalues of the system. As discussed in [17], for a triangular unstructured grid, this can be formulated:

$$\Delta t_{max} = \min\left\{\Delta t_k^{CFL}\right\}_{k=1,Nedge}$$
$$\Delta t_k^{CFL} = \min_{1\leqslant m\leqslant 3+p}\left\{\frac{A_{min,k}}{\max\left[\left|\tilde{\lambda}_k^m\right|\right] l_k}\right\} \tag{48}$$

with $A_{min,k} = \min(A_i, A_j)$ and *Nedge* the number of cell edges in the domain.

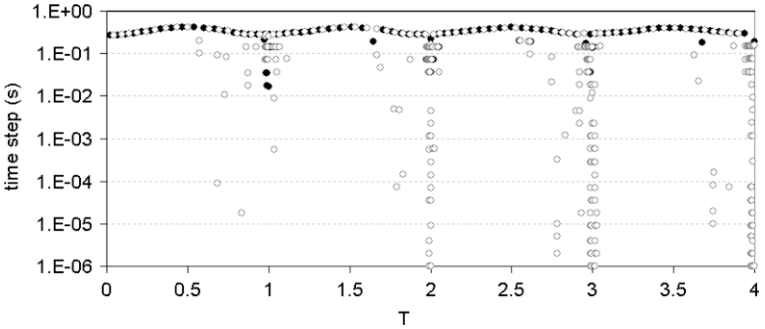

Fig. 7. Time step size distribution (logarithmic scale) during the computation of four periods in test 1 for case 1 (black dots) and case 7 (white dots).

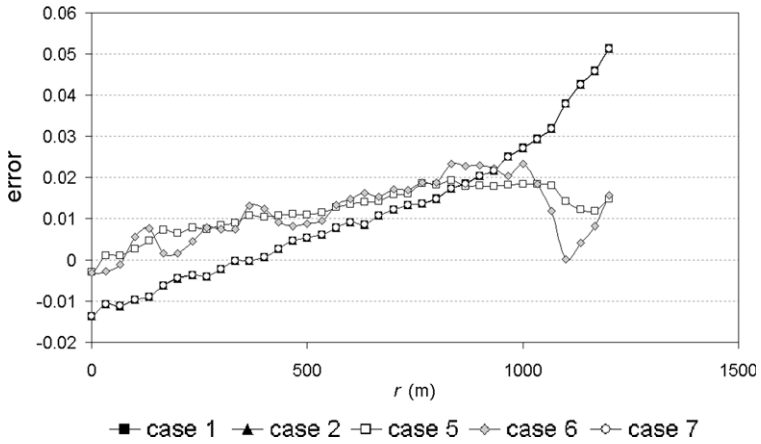

Fig. 8. Error in the numerical solution for ϕ_1 at time $4T$ for cases 1, 2 and 5–7.

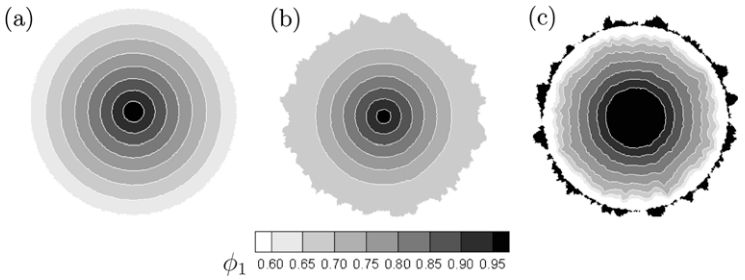

Fig. 9. Contour plot of the exact distribution of ϕ_1 at time $4T$ (a), and computed distribution of ϕ_1 at time $4T$ for options 1 (coupled) and 10 (uncoupled) in (b) and (c), respectively.

This time step limitation is the main disadvantage of explicit schemes and it is worth trying to avoid further restrictions in the time step size dictated by, for instance, the presence of relevant source terms. Having splitted the diffusive and reaction parts, the strategy presented for multi-component transport in this work is based on the redistribution of the updating fluxes $\Psi_{i,k}$ allowing the use of the time step in (48). This idea starts by focusing in the evaluation of the negative mass contributions to a cell, and the value of the maximum allowable time step (48). Given a wet cell i, the contributions from neighbour cells that extract mass are used to build a reference time step size Δt_{h_i}:

$$\Delta t_{h_i} = -\frac{h_i^n}{\Delta t \sum_{k=1}^{NE} \Psi_{i,k}^h}, \quad \Psi_{i,k}^h < 0 \tag{49}$$

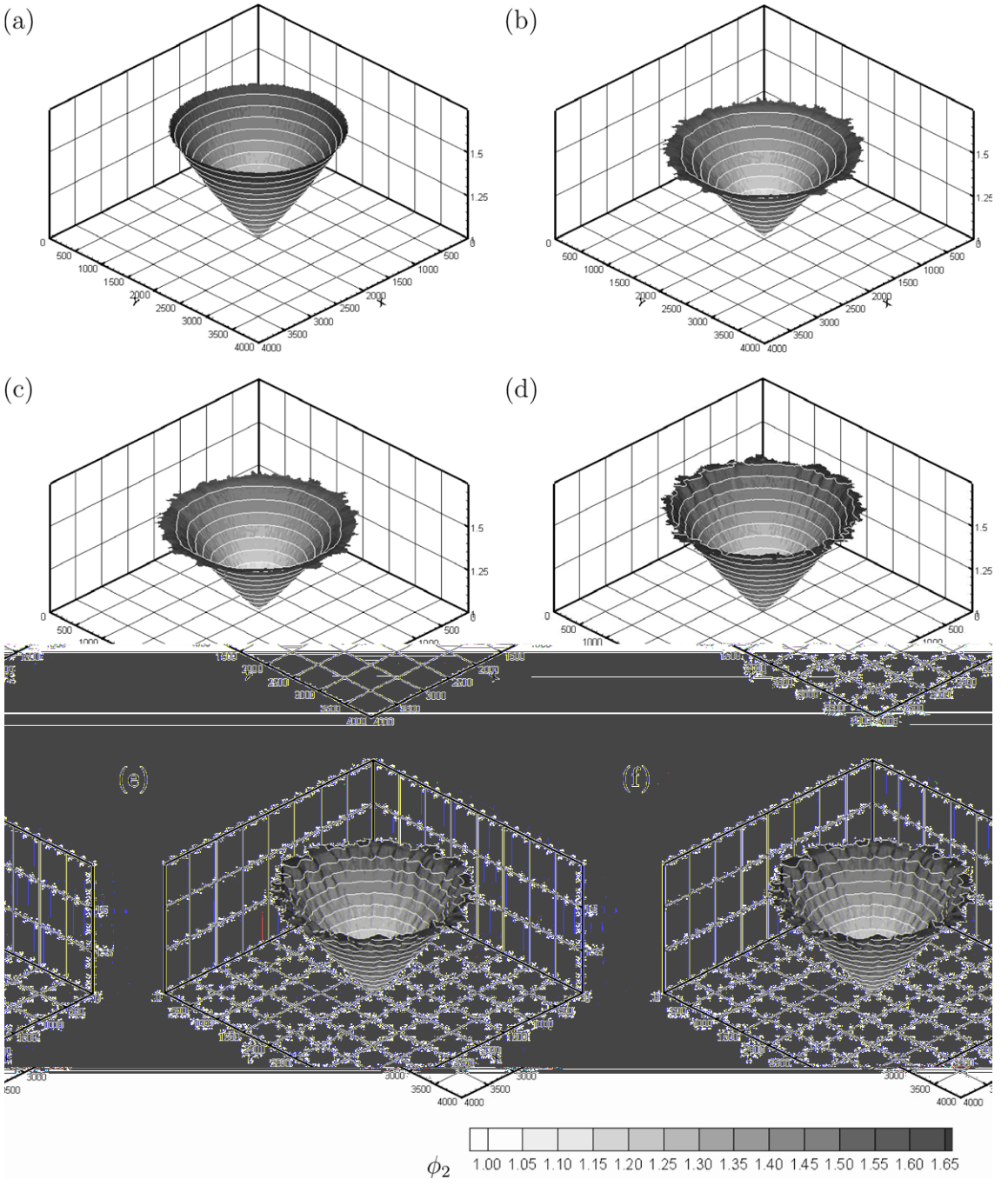

Fig. 10. 3D view of the exact distribution of ϕ_2 at time $4T$ (a), and computed distribution of ϕ_2 at time $4T$ for cases 1, 3 and 5–7 in (b)–(f), respectively.

The same is repeated for the mass conservation equations of all the components $h\phi_s$ and new reference time steps $\Delta t_{h\phi_{s,i}}$ are estimated:

$$\Delta t_{h\phi_{s,i}} = -\frac{h\phi^n_{s,i}}{\Delta t \sum_{k=1}^{NE} \Psi^{h\phi^n_{s,i}}_{i,k}}, \quad \Psi^{h\phi_{s,i}}_{i,k} < 0 \tag{50}$$

It is worth noting that the quantities defined in (49) and (50) are always positive due to the condition on the contributions in the denominator. A redistribution factor is computed as:

$$\begin{aligned} r_{t,i} &= \frac{\Delta t_v}{\Delta t_{max}} \\ \Delta t_v &= \min\left(\Delta t_{max}, \Delta t_{h_i}, \Delta t_{h\phi_{1,i}}, \Delta t_{h\phi_2}, \ldots, \Delta t_{h\phi_{p,i}}\right) \end{aligned} \tag{51}$$

with Δt_{max} as in (48). When in cell i the ratio $r_{t,i} < 1$, we propose to redefine the updating fluxes to cells i and j at those k edges where $\Psi^h_{k,i} < 0$ according to:

$$\begin{aligned} \boldsymbol{\Psi}_{i,k} &= \boldsymbol{\Upsilon}_{\mathbf{1}}, \quad \boldsymbol{\Psi}_{j,k} = \boldsymbol{\Psi}_{j,k} + \boldsymbol{\Upsilon}_{\mathbf{2}} \\ \Psi^{hu}_{i,k} &= \Psi^{hv}_{i,k} = 0 \end{aligned} \tag{52}$$

where

$$\boldsymbol{\Upsilon}_{\mathbf{1}} = \boldsymbol{\Psi}_{i,k} r_{t,i}, \quad \boldsymbol{\Upsilon}_{\mathbf{2}} = \boldsymbol{\Psi}_{i,k}(1 - r_{t,i}) r_A \tag{53}$$

imposing a condition of zero velocity in the normal direction to the cell edge where $\Psi^h_{k,i} < 0$ to preserve conservation in the following time step. In this technique the flux components are homogeneously redefined in order to ensure a correct bounding of the transported scalars. It is worth remarking that the strategies defined in Section 3.3 are indispensable to apply the flux conservative redistribution successfully.

In previous works [15] the transport of one single scalar was considered and the effect of the edge redistribution in (47) was supplied by the cell redistribution in (52). In the context of multivariable transport, if the edge redistribution techniques (46) and (47) are not observed, it is not possible to avoid negative values of solute for any size of the time step, as the $r_{t,i}$ factor cannot handle all the variety of possible combinations and the computation fails.

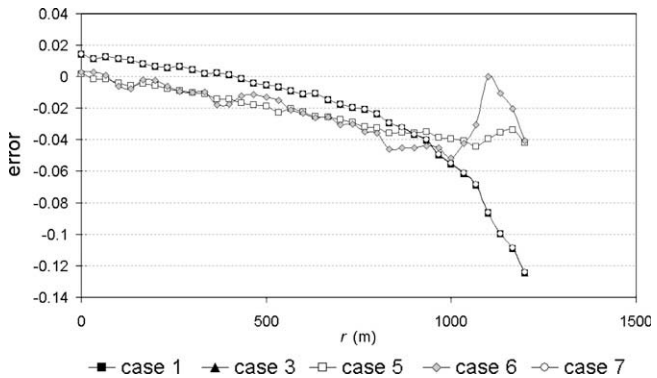

Fig. 11. Error in the numerical solution for ϕ_2 at time $4T$ for cases 1, 3 and 5–7.

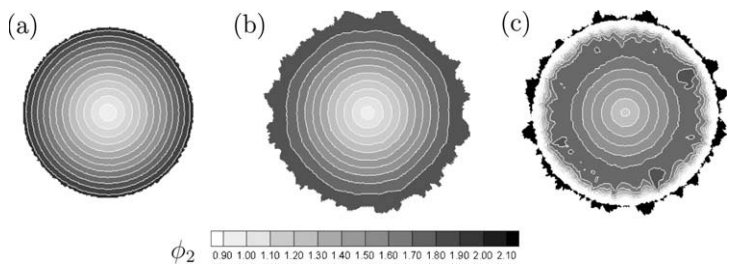

Fig. 12. Contour plot of the exact distribution of ϕ_2 at time $4T$ (a), and computed distribution of ϕ_2 at time $4T$ for options 1 (coupled) and 10 (uncoupled) in (b) and (c), respectively.

When moving to the second order approach in (41) the cell redistribution strategy presented in this section can also be applied to multivariable transport. To do that, it is necessary to observe the results of the analysis of the influence of the non-conservative terms in the stability region [17,18]. One main conclusion, was that the size of the actual time step in presence of relevant source terms involves more variables than the ones defined in (48). When analysing systems of Eq. (1) the following edge parameter is additionally relevant:

$$\gamma_k = \min\{\gamma_h, \gamma_{h\phi_1}, \gamma_{h\phi_2}, \ldots, \gamma_{h\phi_{3+p}}\}_k \tag{54}$$

where for any U conserved variable, $\gamma_{U,k}$ is

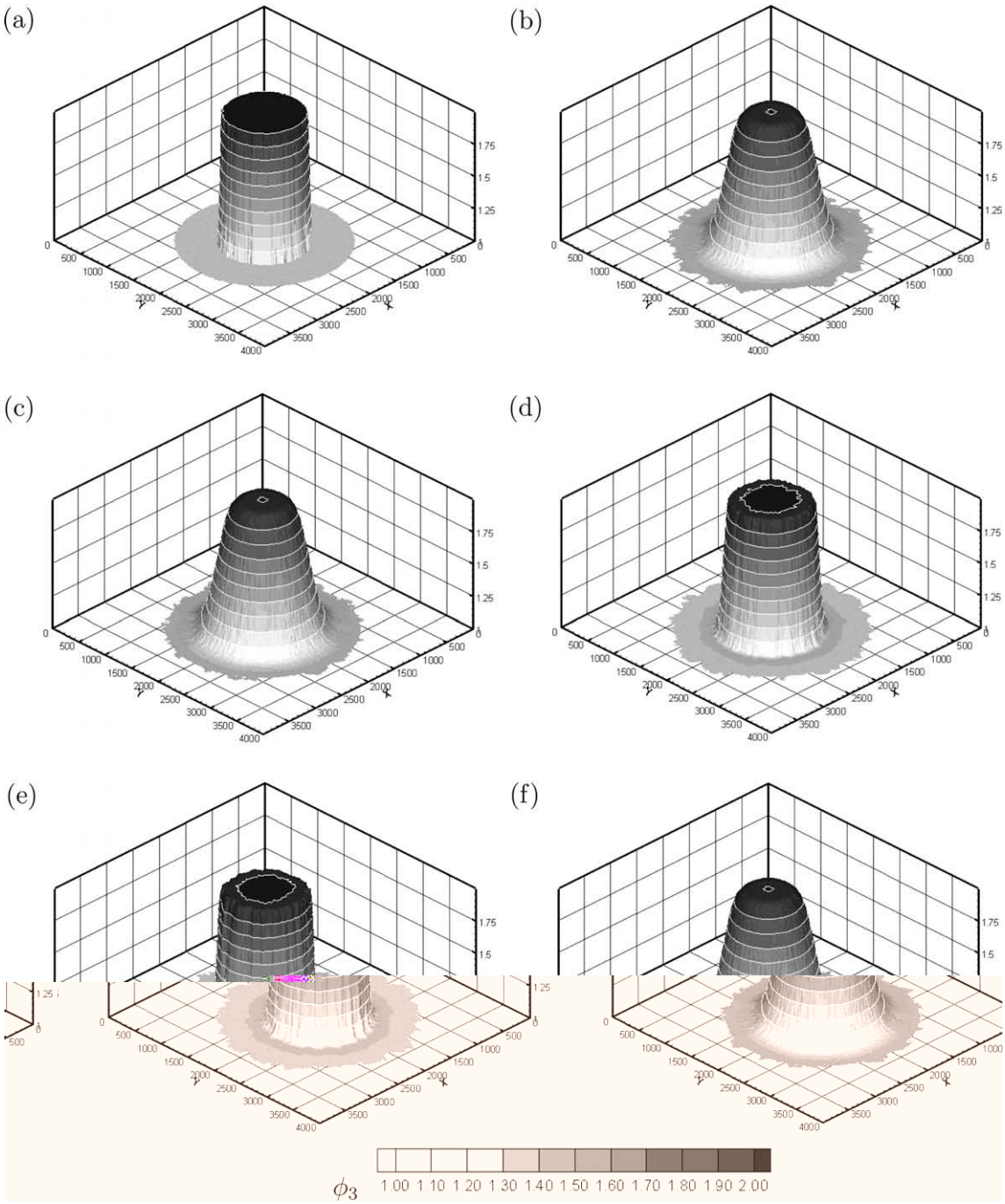

Fig. 13. 3D view of the exact distribution of ϕ_3 at time $4T$ (a), and computed distribution of ϕ_3 at time $4T$ for cases 1 and 4–7 in (b)–(f), respectively.

$$\gamma_{U,k} = \frac{\min\{U_i, U_j, |\delta U_k|\}}{|\delta U_k|} \tag{55}$$

This parameter is related to the monotonicity of the initial values in each Riemann problem, and does not affect the stability in presence of non-conservative products in the case $\gamma_k = 1$. Otherwise, when $\gamma_k < 1$ the time step in (48) must be reduced. The conservative flux redistribution avoids this problem, but when moving to second order in space, to preserve the optimization in the size of the time, in those cells where $\gamma_k < 1$ for any k edge, first order is locally imposed for all variables in the cell.

Also, in second order the techniques in (46) and (47) must be considered over the $\Psi^{h\phi_s}_{Jl,k}$ fluxes, to avoid time size independent problems. It is remarkable that in second order in time and space the maximum time step changes [27], and is given by

$$\begin{aligned} \Delta t_{max} &= \frac{2}{3} \min\left\{\Delta t_k^{CFL}\right\}_{k=1,Nedge} \\ \Delta t_k^{CFL} &= \min_{1\le m\le 3+p} \left\{ \frac{A_{min,k}}{\max\left[\left|\tilde{\lambda}_k^m\right|\right] l_k} \right\} \end{aligned} \tag{56}$$

Finally, it has been previously reported that explicit discretizations of the friction term, unified (upwind) and separated (pointwise), lead to instabilities in cases of dominant roughness, that can be avoided by reducing the time step in (48) or the cell size [17,19]. Implicit discretizations of this term have been widely used to overcome this problem, but are unable to ensure well-balanced steady state solutions. A technique that combines the implicit pointwise and the explicit upwind friction discretization proposed in [19] is adopted here, leading to computationally efficient simulations by means of an adequate criterion that switches from one to the other whilst remaining under the solely control of the time step condition in (48).

3.5. Uncoupled formulation for solute transport

Solving solute transport by means of an uncoupled formulation is an option commonly used, that may lead to numerical issues in some cases, as will be shown later. The system of equations in (1) is divided in two different sub-systems of equations, one for the mass and momentum shallow water equations

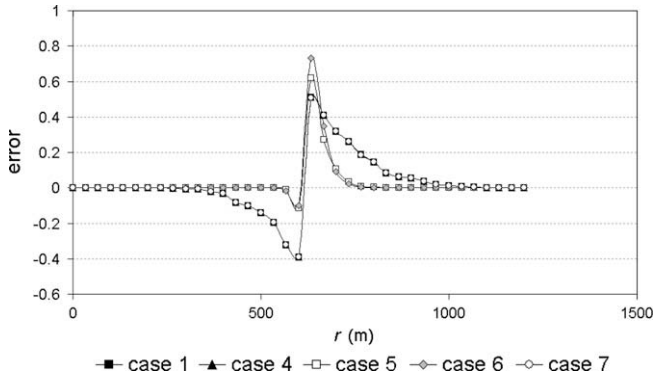

Fig. 14. Error in the numerical solution for ϕ_3 at time $4T$ for cases 1 and 4–7.

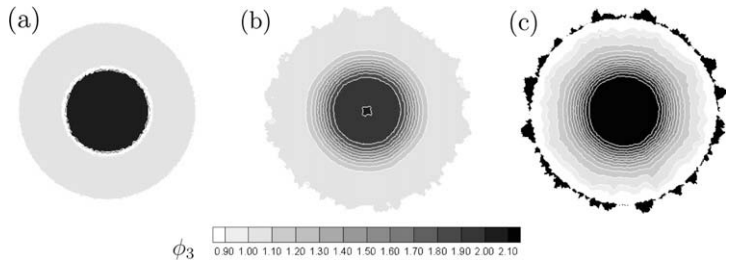

Fig. 15. Contour plot of the exact distribution of ϕ_3 at time $4T$ (a), and computed distribution of ϕ_3 at time $4T$ for options 1 (coupled) and 10 (uncoupled) in (b) and (c), respectively.

$$\frac{\partial \mathbf{U}_1}{\partial t} + \frac{\partial \mathbf{F}_1(\mathbf{U})_1}{\partial x} + \frac{\partial \mathbf{G}_1(\mathbf{U})_1}{\partial x} = \mathbf{S}(\mathbf{U})_1 + \vec{\nabla}\mathbf{D}_1(\mathbf{U})_1 \tag{57}$$

where $\mathbf{U} = (h \quad hu \quad hv)^T$ and another for the mass conservation of the transported components

$$\frac{\partial \mathbf{W}}{\partial t} + \frac{\partial \mathbf{F}_2(\mathbf{W})}{\partial x} + \frac{\partial \mathbf{G}_2(\mathbf{W})}{\partial x} = \vec{\nabla}\mathbf{D}_2(\mathbf{W}) + \mathbf{R}(\mathbf{W}) \tag{58}$$

with $\mathbf{W} = \left(h\phi_1 \quad h\phi_2 \quad \cdots \quad h\phi_p\right)^T$

The sub-systems are solved independently and sequentially with any of the available methods. In the present work, the comparisons between the coupled and the uncoupled formulations will be based on the application of the upwind finite volume methods discussed in previous sections using the reduced Jacobians corresponding to each sub-system. The following

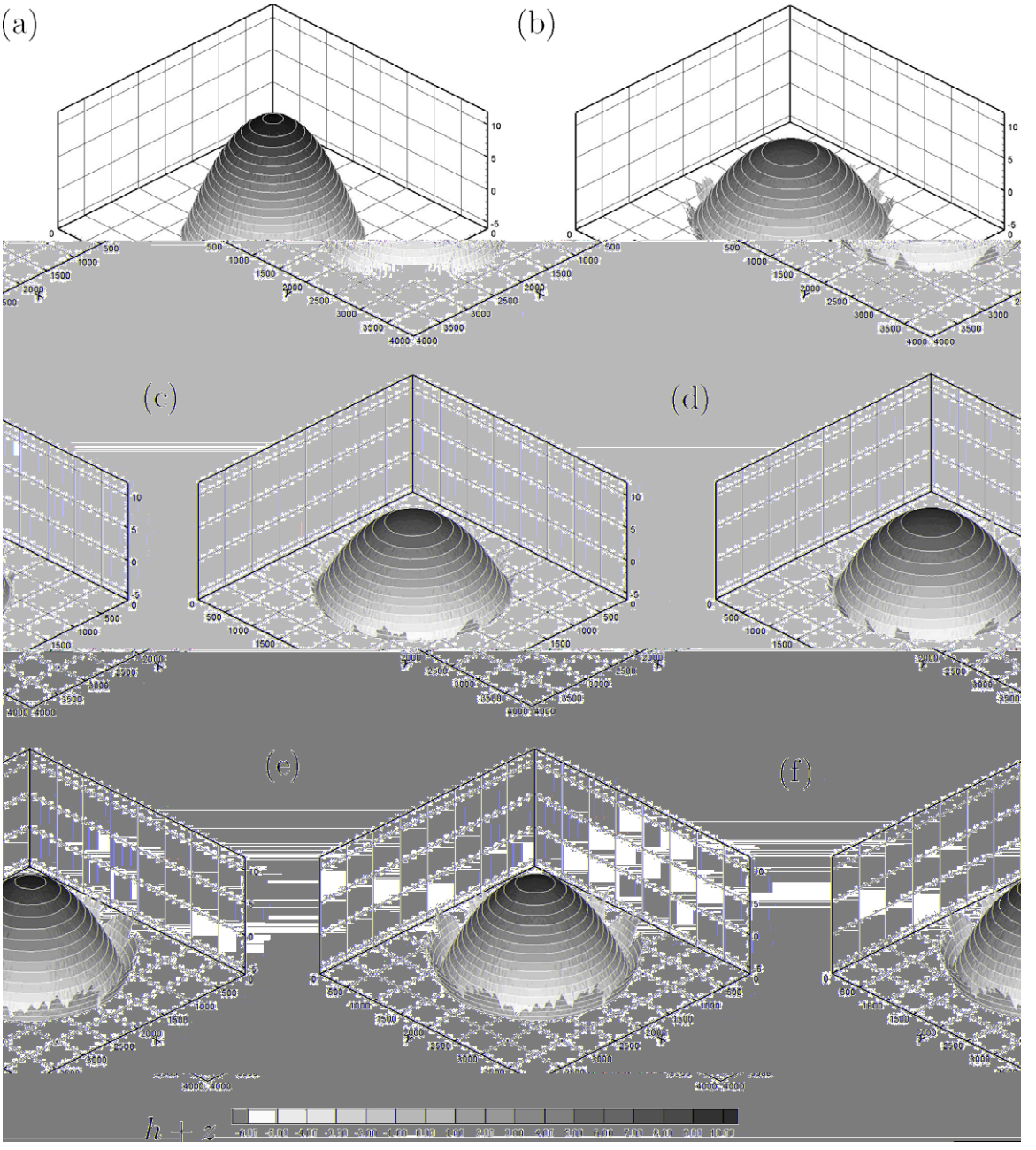

Fig. 16. 3D view of the exact water level surface at time $4T$ (a), and computed water level surface at time $4T$ for cases 1, 5 and 7–9 in (b)–(f), respectively.

formulation defines the application of the first order upwind scheme to the convective part of sub-system (58) and has been widely reported [7,10]:

$$\mathbf{W}_i^* = \mathbf{W}_i^n + \Delta t \sum_{k=1}^{NE} (\bar{\mathbf{u}}\mathbf{n})_k^{-n} \delta \mathbf{W}_k \frac{l_k}{A_i} \tag{59}$$

with $(\bar{\mathbf{u}})^- = \frac{1}{2}(\bar{\mathbf{u}} - |\bar{\mathbf{u}}|)$ and $\bar{\mathbf{u}} = \frac{1}{2}(\mathbf{u}_i + \mathbf{u}_j)$.

4. Applications

4.1. Long wave resonance in a circular parabolic frictionless basin with solute

The first test case presented is motivated by the necessity of checking the performance of flux redistributions proposed when using the schemes in (29) and (41) in a problem of transient boundaries dominated by the non conservative terms and with analytical solution. The analytical solution of a long wave resonating in a circular, frictionless parabolic basin was presented in [26] for the shallow water equations, and is taken as the basis of our test case. The free surface displacement is given by

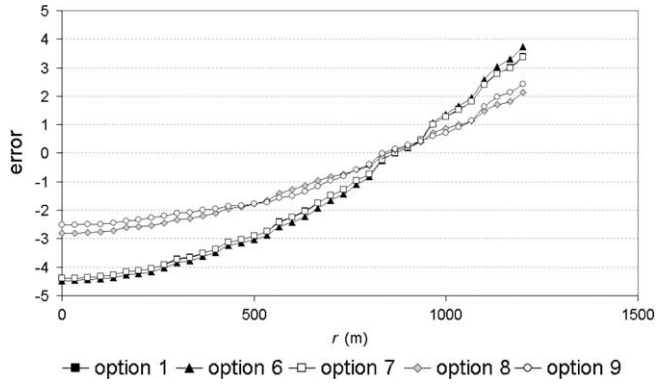

Fig. 17. Error in the numerical solution for $h + z$ at time $4T$ for cases 1 and 6–9.

Table 2
L_1 and L_∞ errors for ϕ_1 and ϕ_2 for 1D convergence to steady state with ω variable.

Option	$L_1(\phi_1)$	$L_\infty(\phi_1)$	$L_1(\phi_1)$	$L_\infty(\phi_2)$
Explicit	0.192396	0.013782	0.192396	0.013782
Implicit	0.190070	0.012228	0.190070	0.012228

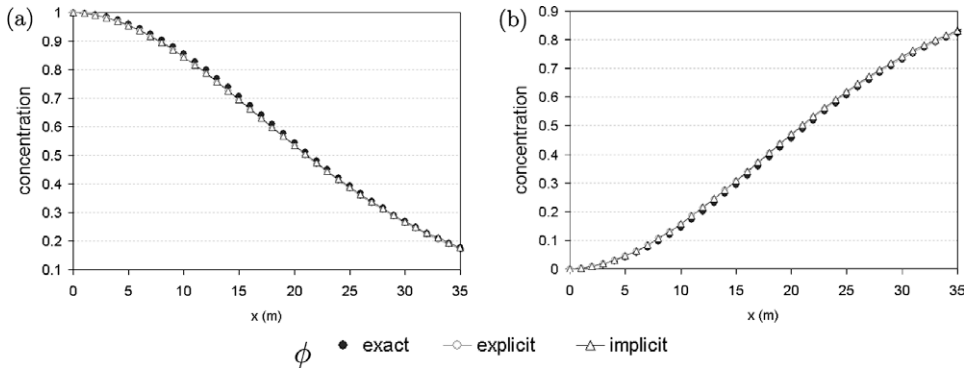

Fig. 18. Detail of the steady state solution for ϕ_1 (a) and for ϕ_2 (b) using the explicit and the implicit discretization of the reaction terms.

$$\zeta(r,t) = \zeta_o\left(\frac{(1-A^2)^{1/2}}{1-A\cos\omega t} - 1 - \frac{r^2}{a^2}\left(\frac{1-A^2}{(1-A\cos\omega t)^2} - 1\right)\right) \tag{60}$$

and the basin shape is given by

$$z(r,t) = \zeta_o\left(1 - \frac{r^2}{A^2}\right) \tag{61}$$

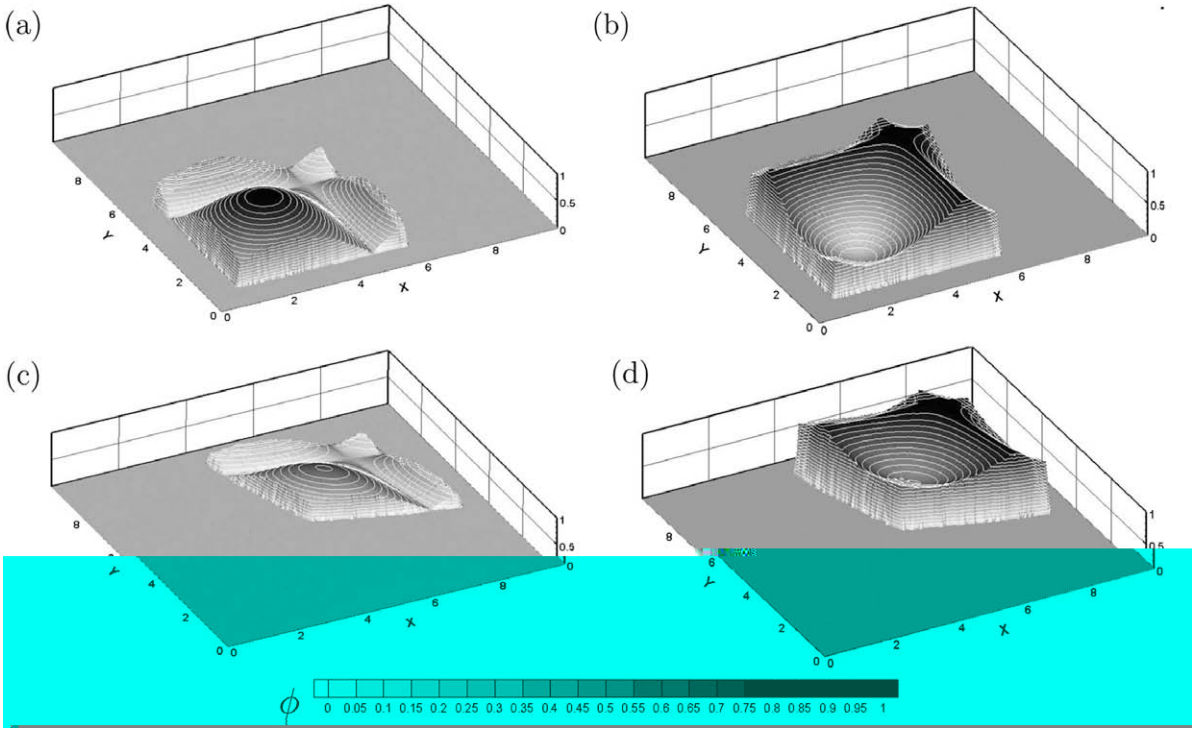

Fig. 19. 3D contour plot for ϕ_1 and ϕ_2 at time $t = 0$ in (a) and (b), respectively. 3D contour plot for the analytical solutions for ϕ_1 and ϕ_2 at time $t = 50$ s in (c) and (d), respectively.

Table 3
Summary of numerical options for the 2D unsteady state.

Option	Interpolated variable	Reaction discretization	Coupled system
1	No one	Explicit	Yes
2	$\phi_1,\ \phi_2$	Explicit	Yes
3	$q_x,\ q_y,\ \phi_1,\ \phi_2$	Explicit	Yes
4	No one	Implicit	Yes
5	$\phi_1,\ \phi_2$	Implicit	Yes
6	$q_x,\ q_y,\ \phi_1,\ \phi_2$	Implicit	Yes
7	No one	Explicit	No

Table 4
L_1 and L_∞ errors for ϕ_1 and ϕ_2 for 2D unsteady state.

Option	$L_1(\phi_1)$	$L_\infty(\phi_1)$	$L_1(\phi_1)$	$L_\infty(\phi_2)$
1	1.222263	0.235186	3.199296	0.684575
2	0.395466	0.214274	1.116122	0.681365
3	0.396762	0.214833	1.120822	0.684299
4	1.222239	0.235184	3.199294	0.684576
5	0.396025	0.211760	1.116283	0.681492
6	0.396883	0.215342	1.118067	0.682741
7	2.127666	0.291585	6.233282	0.723769

with $A = (a^4 - r_o^4)(a^4 + r_o^4)$ and $\omega = a^{-1}\sqrt{8g\zeta_o}$, where ζ_o is the centre point water depth, r is the distance from the centre point, a is the radial distance from the centre point to the zero elevation on the shoreline and r_o is the distance from the centre point to the point where the water depth is initially nil. Those values are represented in Fig. 5. The numerical values used for this test are $\zeta_o = 20.0$ m, $r_o = 1200$ m, $a = 1500$ m. $T = 2\pi\omega^{-1} = 237.93$ s. The domain is divided in 52,242 unstructured triangular cells for the comparisons and does not present any adaptation to the bottom surface. The basic test case has been extended by assuming that the water surface movement transports, in a purely advective form, three initial solute ($p = 3$) concentrations. There is no analytical solution for the solute concentration evolution in time but, in absence of diffusion, the solution is provided by the analytical velocity field, hence, for each T oscillation period, the solute concentration will be:

$$\phi(r, t = KT) = \phi(r, t = 0), \quad K = 1, \ldots, \infty \tag{62}$$

To compare exhaustively the performance of the numerical techniques detailed in this work, 10 different numerical cases, involving different initial solute distributions and different numerical options have been defined. The cases are summarized in Table 1. In all cases the initial solute distribution for each transported variable is given by the functions

$$f_1 = e^{\left(\frac{-2r}{r_o}\right)}, \quad f_2 = e^{\left(\frac{2r}{r_o}\right)}, \quad f_3 = \begin{cases} 2 & \text{if } r < 600 \\ 1 & \text{if } r \geqslant 600 \end{cases} \tag{63}$$

or is simply nil in the entire domain. Cases 1–4 have been defined to compare the effect of the conservative redistribution in the solution, using the first order scheme for that purpose. It is expected that the solutions for the transported scalars remain identical in all cases, despite the fact of being present in the computation or not. In cases 5 and 6 second order over the transported scalars and over the transported scalars and the discharges, respectively, is applied using (41) in combination with the conservative redistribution. Case 7 is the reference case when first order is applied, the conservative flux redistribution in (52) is not used and the time step size in (48) is reduced until no value of the solute concentration becomes negative. Cases 8 and 9 have been defined to show the performance of the scheme in (41) when interested in preserving the initial water level surface profile as in case 6. Case 10 uses the uncoupled formulation in (59) for the transported scalars.

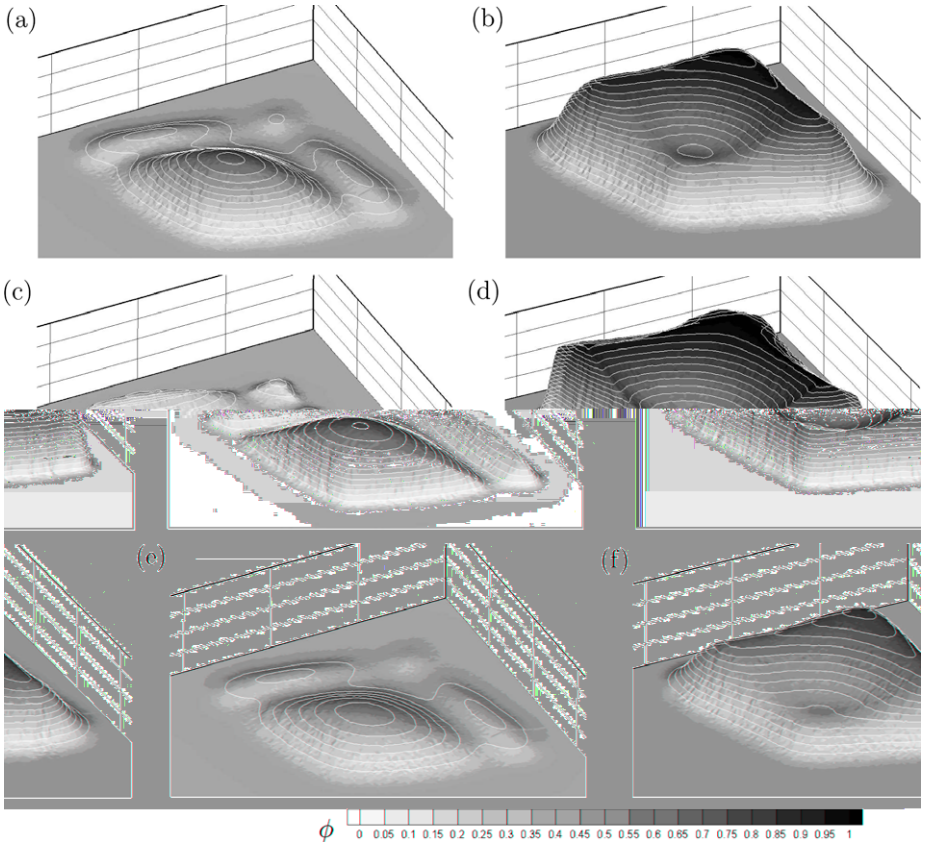

Fig. 20. 3D contour plot of the numerical solution for ϕ_1 and ϕ_2 at time $t = 50$ s using option 1 in (a) and (b), respectively, using option 2 in (c) and (d), using option 7 in (e) and (f), respectively.

Fig. 6 shows 3D views of (a) the exact distribution of ϕ_1 at time $4T$, and (b)–(f) computed distribution of ϕ_1 at time $4T$ for cases 1, 2 and 5–7, respectively. From Fig. 6(b), (c) and (f) it can be observed that the simulation of the transport of three mutually independent components provides the same result as the simulation of that single component alone both when the flux redistribution is performed and when it is not. However, the flux redistribution helps in ensuring stability at higher time step sizes, as shown in Fig. 7. Fig. 6(d) and (e) show that there is a gain in accuracy when moving to second order. Despite the strong variation of the wet computational domain during the simulation, the solution preserves the symmetry of the original solution. The deviation from the exact solution, at a row of points along a radius after 4 periods, is quantitatively compared in Fig. 8, where the difference between the numerical and the exact solution is plotted. Cases 1, 2 and 7 provide the same error. The extra computational effort made when involving interpolation techniques for the velocity in case 6 is not justified in this case. The influence of the coupling in the system can be observed by comparing options 1 and 10. This is displayed on Fig. 9 for the component ϕ_1 together with the exact solution at $t = 4T$. The solution from the uncoupled formulation is not bounded and does not follow the correct pattern at any time.

Fig. 10 are 3D views of (a) the exact distribution of ϕ_2 at time $4T$ and (b)–(f) the computed distribution of ϕ_2 at time $4T$ for options 1, 3 and 5–7, respectively. The difference between the numerical and the exact solution is plotted in Fig. 11. Cases 1, 3 and 7 provide the same error. The extra computational effort made involving interpolation techniques for the velocity in case 6 is not justified in this case. There is a gain in accuracy when moving to second order but again it is not worth enforcing second order in the discharges as far as the error in concentration is concerned. Fig. 12(a) is the contour plot of the exact distribution of ϕ_2, at time $4T$ and Fig. 12(b) and (c) are the corresponding numerical solutions computed with options 1 and 10, respectively.

Fig. 13 are 3D views of the exact distribution of ϕ_3 at time $4T$ (a), and computed distribution of ϕ_3 for options 1, and 4–7 in (b)–(f), respectively, at the same time. The difference between the numerical and the exact solution is plotted in Fig. 14. Fig. 15(a) shows the contour plot of the exact distribution of ϕ_3 at time $4T$, and the computed distributions of this variable for options 1 and 10 are represented in 15(b) and (c), respectively.

Fig. 16 complements all the previous and shows the comparison of the exact and computed water level surfaces at time $t = 4T$ in 3D view. All the computed water surfaces are smooth and symmetric. Fig. 17 is a quantitative comparison of the exact solution and the numerical water surface level solutions. Cases 1 and 7 provide the same error, close to that obtained in case 6, reinforcing that second order over the discharges does not improve the water level solution. There is a gain in accuracy when moving to second order but it would be enough to use second order over the water depth.

4.2. Application to solute transport with reaction

The second test case is intended to focus on the reactive source terms. For that purpose, the transport of two interdependent components ($p = 2$) is formulated defining **R** and **D** as follows:

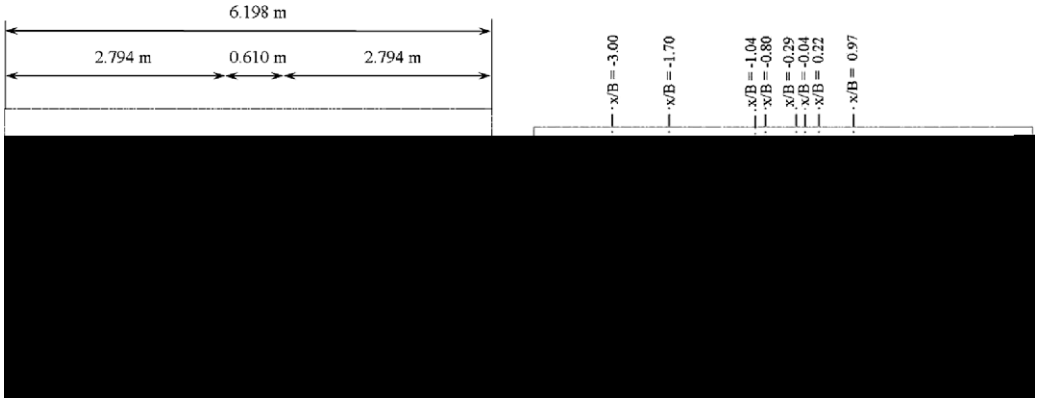

Fig. 21. (a) Experimental channel for dividing flow and (b) data collection sections.

Table 5
Summary of computational options in the 90° dividing open channel flow.

Option	Interpolation variable	Turbulence model	Gradient discretization
1	No one	No	Centred plane
2	No one	Yes	Centred plane
3	q_x, q_y	Yes	Centred plane
4	κ, ϵ, q_x, q_y	Yes	Centred plane
5	No one	Yes	Normal discretization
6	No one	Yes	Max. gradient plane

$$\mathbf{R} = (\,0 \quad 0 \quad 0 \quad -\omega h\phi_1 \quad \omega h\phi_2\,)^T, \quad \mathbf{D} = 0 \tag{64}$$

and two situations are identified.

4.2.1. 1D convergence to steady state with ω variable

The exact solution for the solute distributions in steady state conditions is obtained from the solute transport equation written as:

$$\vec{\nabla} h\mathbf{u}\phi_1 = -\omega h\phi_1, \quad \vec{\nabla} h\mathbf{u}\phi_2 = \omega h\phi_1 \tag{65}$$

To isolate the effect of the discretization of the reaction terms, a 1D flat and frictionless channel, with uniform and constant flow values, h_o and q_o, and length L is considered. Eq. (65) reduces to

$$\mathbf{u}\vec{\nabla}\phi_1 = -\omega\phi_1, \quad \mathbf{u}\vec{\nabla}\phi_2 = \omega\phi_1 \tag{66}$$

If the boundary conditions for the scalars transported are $\phi_1(x=0) = \chi$ and $\phi_2(x=0) = 1-\chi$ and

$$\omega(x) = \omega_o \sin\left(\frac{\pi x}{L}\right) \tag{67}$$

the steady state solution is

$$\phi(x) = \chi e^{\left(-\frac{\omega_o L}{u\pi}\left(1-\cos\left(\frac{2\pi x}{L}\right)\right)\right)} \tag{68}$$

The computational problem is defined using $L = 100$ m, $h_o = 1$ m, $q_o = 1$ m^2/s, $\chi = 1$, $\omega_o = 0.1$ s^{-1} and initial conditions $\phi_1(x, t=0) = \phi_2(x, t=0) = 0$. The upstream and downstream imposed conditions are

$$q(x=0) = q_o, \quad \phi_1(x=0) = \chi, \quad \phi_2(x=0) = 1-\chi, \quad h(x=L) = h_o \tag{69}$$

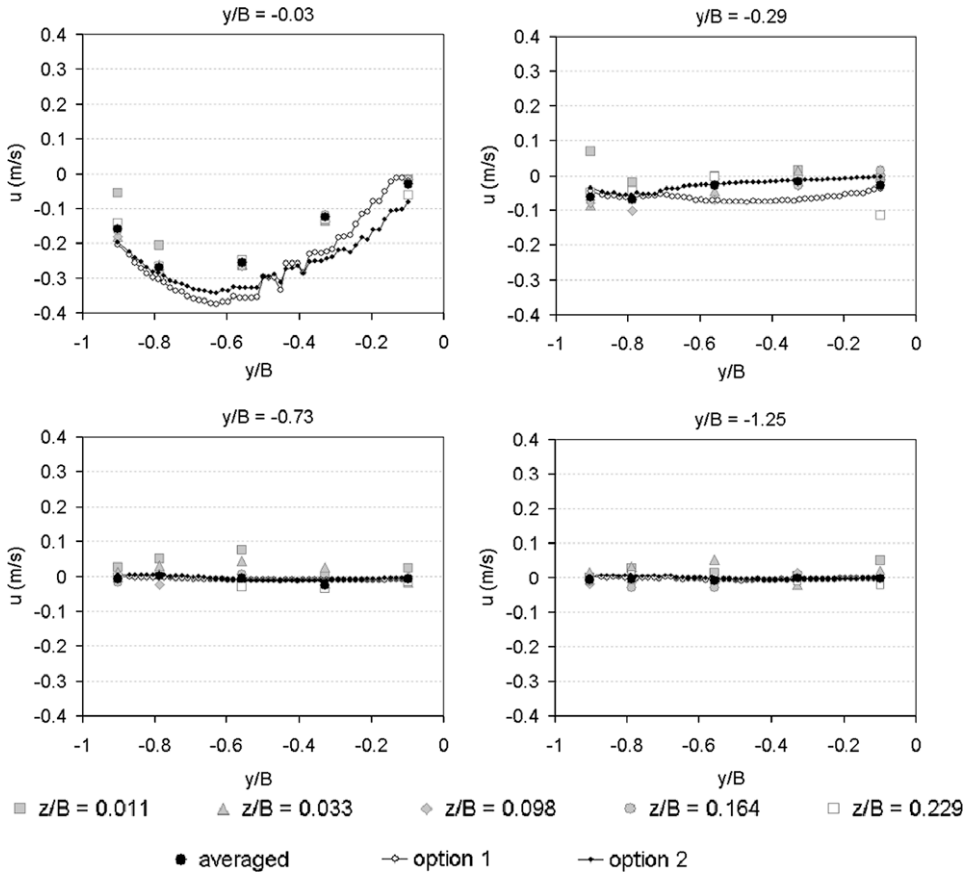

Fig. 22. Velocity u measured at different water depths ($z/B = 0.011$, $z/B = 0.033$, $z/B = 0.098$, $z/B = 0.164$, $z/B = 0.229$), depth average of the velocity measurements and computed velocity in options 1 and 2.

Table 2 displays the L_1 and L_∞ errors for ϕ_1 and ϕ_2 at steady state, showing that both the explicit and implicit discretizations of the reaction terms provide the same accuracy in this case. Fig. 18 is a detail of the steady state solution for ϕ_1 (a) and for ϕ_2 (b) using the explicit and implicit schemes. This example involves a smooth solution over a flat bottom with uniform free surface, hence, both the coupled and uncoupled formulation lead to the same results.

4.2.2. 2D unsteady transport

The second case of transport with reaction considers unsteady solutions. From the solute transport equation and the water mass conservation, the material derivatives can be written:

$$\begin{aligned} \frac{d\phi_1}{dt} &= -\omega\phi_1, \quad \frac{dx}{dt} = u \\ \frac{d\phi_2}{dt} &= \omega\phi_1, \quad \frac{dx}{dt} = v \end{aligned} \tag{70}$$

The test case is concerned with the advection and reaction of an initial solute distribution by means of the velocity field corresponding to a non-uniform steady flow characterized by a bi-linear bed variation. The exact water depth and bottom level distributions corresponding to that situation are:

$$h(x,y) = a + q_x x + q_y y, \quad z(x,y) = -\frac{1}{2g}\frac{q_x^2 + q_y^2 + 2gh^3}{h^2} + \frac{3}{7}\frac{|q_x| n^2 \sqrt{2}}{h^{7/3}} \tag{71}$$

$q_x = q_y = cte$, which means that the solute concentrations vary along the characteristic curves given by

$$\frac{dx}{dt} = \frac{q_x}{h(x,y)}, \quad \frac{dy}{dt} = \frac{q_y}{h(x,y)} \tag{72}$$

Assuming that at the initial time t_o the solute distributions hold

$$\phi_1(x_o, y_o, t_o) + \phi_2(x_o, y_o, t_o) = \chi \tag{73}$$

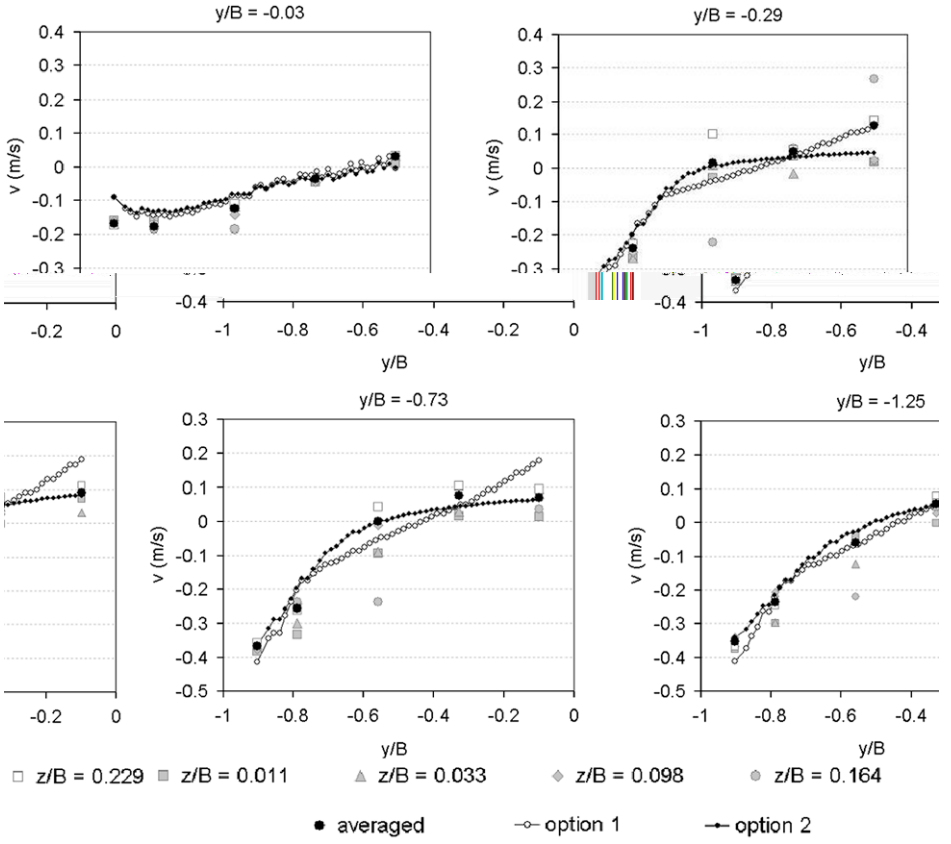

Fig. 23. Velocity v measured at different water depths ($z/B = 0.011$, $z/B = 0.033$, $z/B = 0.098$, $z/B = 0.164$, $z/B = 0.229$), depth average of the velocity measurements and computed velocity in options 1 and 2.

the concentrations at a future time $t_o + T$ change along the space according to:

$$\begin{aligned}\phi_1(x', y', t_o + T) &= \phi_1(x_o, y_o, t_o)e^{-\omega T} \\ \phi_2(x', y', t_o + T) &= \chi - \phi_1(x_o, y_o, t_o)e^{-\omega T}\end{aligned} \tag{74}$$

where

$$x'(t_o + T) = x_o(t_o) + \int_{t_o}^{t_o+T} u\,dt, \quad y'(t_o + T) = y_o(t_o) + \int_{t_o}^{t_o+T} v\,dt \tag{75}$$

that, using the field characteristics in (71) become

$$\begin{aligned}x'(t_o + T) &= \left(-A + \sqrt{A^2 + 2BC}\right)B^{-1} \\ y'(t_o + T) &= y_o + q_y q_x^{-1}\left(\left(-A + \sqrt{A^2 + 2BC}\right)B^{-1} - x_o\right)\end{aligned} \tag{76}$$

with $A = a + q_y y_o - q_y^2 q_x^{-1} x_o$, $A = q_x + q_y^2 q_x^{-1}$, $C = Ax_o + \frac{1}{2}Bx_o^2 + q_x(t_o + T)$.

The example presented assumes a diagonal discharge with values $q_x = q_y = 0.1\ \mathrm{m^2/s}$, $a = 0.5$ m, roughness $n = 0.03\ \mathrm{s\,m^{-1/3}}$ and $\chi = 1$, over a squared domain 10×10 m, and has been computed using 52,242 unstructured triangular cells. The boundary conditions are, at the upstream sides (south and west in the squared domain), the unit discharges and, at the downstream sides (north and east), the water depth. No diffusion is included. The initial condition for the transported scalars is

$$\phi_1(x, y, t_o) = \begin{cases} \left|\sin\left(\frac{2\pi x}{L}\right)\sin\left(\frac{2\pi y}{L}\right)\right| & \text{if } 1 < x < 6 \text{ and } 1 < y < 6 \\ 0 & \text{otherwise} \end{cases} \tag{77}$$

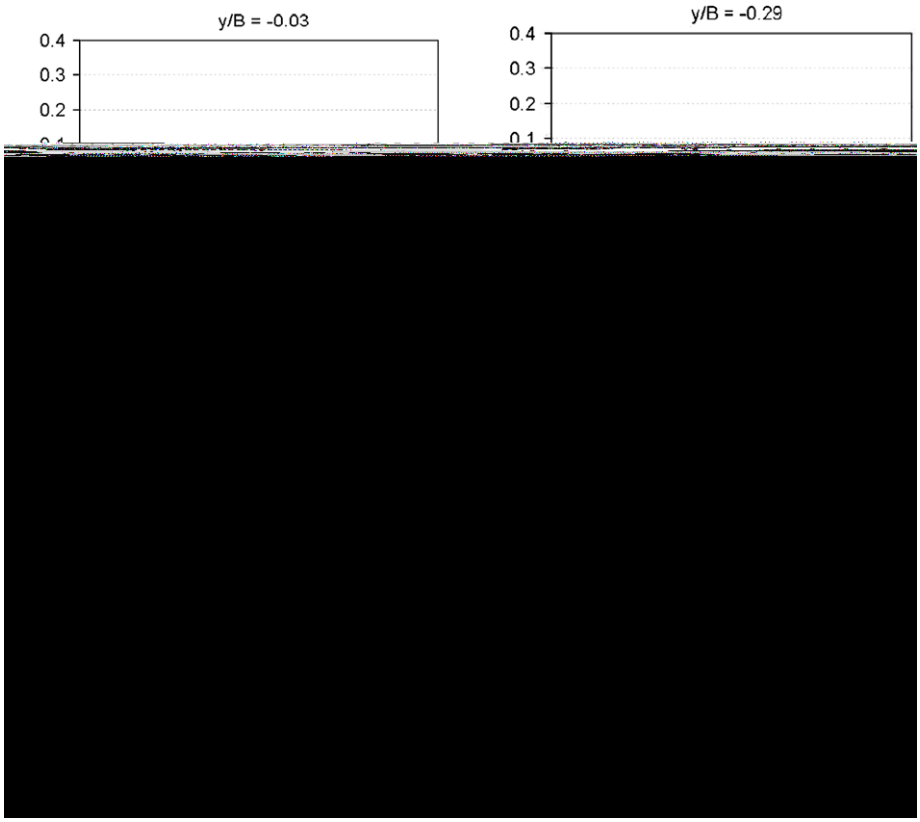

Fig. 24. Depth averaged measured velocity u and computed velocity in options 2 and 3.

Fig. 19 is a 3D plot of the initial and exact solution for ϕ_1 and ϕ_2 at $T = 50$ s. This test case has been simulated with seven different computational options that are listed in Table 3 in order to compare their relative performances with the exact solution. Options 1–3 involve an explicit treatment of the reaction term (32) while in options 4–6 an implicit treatment (32) is retained. In option 7 the uncoupled formulation in (59) for solute transport is applied. Table 4 summarizes the L_1 and L_∞ errors for ϕ_1 and ϕ_2 in this case at time $T = 50$ s. The main conclusion is that the uncoupled formulation leads to the most important error. This could even be confused with an excessive numerical damping and could lead to the wrong conclusion that a more accurate advection method is required. Apart from that, within the list of coupled options, second order in the concentrations is effective and the explicit or implicit discretization of the reaction terms is equally efficient. Fig. 20 show 3D contour plots of the numerical solution for ϕ_1 and ϕ_2 at time $T = 50$ s using option 1 in (a) and (b), respectively, using option 2 in (c) and (d), respectively, and using option 7 in (e) and (f), respectively. It is worth remarking that all options have been run including and excluding the conservative flux redistribution to evidence if this technique gets involved unnecessarily. No results are plotted as no difference has been found when comparing the results of both cases.

4.3. Application to turbulence modelling

The multi-component transport can find a field of application in the formulation of the depth averaged $\kappa-\epsilon$ turbulence model. Therefore, following [21] system (1) with $p = 2,\ \phi_1 = \kappa,\ \phi_2 = \epsilon$, being κ the turbulent kinetic energy and ϵ the dissipation rate, is rewritten using the diffusion matrices

$$\mathbf{K}_u = \mathbf{K}_v = \begin{pmatrix} \nu + \nu_t & 0 \\ 0 & \nu + \nu_t \end{pmatrix}$$
$$\mathbf{K}_\kappa = \begin{pmatrix} \nu + \frac{\nu_t}{\sigma_\kappa} & 0 \\ 0 & \nu + \frac{\nu_t}{\sigma_\kappa} \end{pmatrix}, \quad \mathbf{K}_\epsilon = \begin{pmatrix} \nu + \frac{\nu_t}{\sigma_\epsilon} & 0 \\ 0 & \nu + \frac{\nu_t}{\sigma_\epsilon} \end{pmatrix} \tag{78}$$

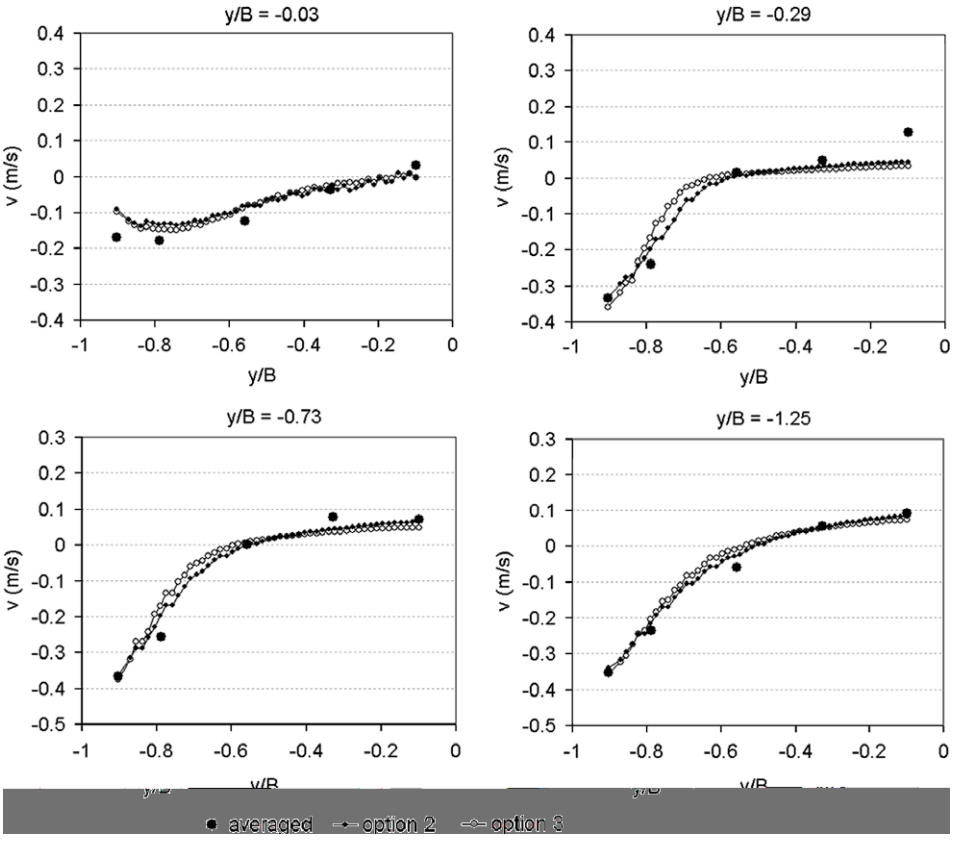

Fig. 25. Depth averaged measured velocity v and computed velocity in options 2 and 3.

The reaction term $\mathbf{R}$ is divided in its positive, $\mathbf{R}_1$, and negative, $\mathbf{R}_2$, terms

$$\begin{aligned}
&\mathbf{R}_1 = \begin{pmatrix} 0 & 0 & 0 & hP_\kappa + hP_{\kappa v} & hc_{1\epsilon}\frac{\epsilon}{\kappa}P_\kappa + hP_{\epsilon,v} \end{pmatrix} \\
&\mathbf{R}_2 = \begin{pmatrix} 0 & 0 & 0 & -h\epsilon & -hc_{2\epsilon}\frac{\epsilon^2}{\kappa} \end{pmatrix} \\
&\nu_t = c_\mu \frac{\kappa^2}{\epsilon}, \quad P_k = 2\nu_t\left(S_{uu}^2 + S_{uv}^2 + S_{vv}^2\right), \quad P_{kv} = \frac{c_k u_f^3}{h} \\
&c_k = \frac{1}{c_f^{1/2}}, \quad P_{\epsilon v} = c_\epsilon \frac{u_f^4}{h^2}, \quad c_\epsilon = 3.6\frac{c_{2\epsilon}c_\mu^{1/2}}{c_f^{3/4}}
\end{aligned} \tag{79}$$

where $c_v = 0.09,\ c_{\epsilon 1} = 1.44,\ c_{\epsilon 2} = 1.92,\ \sigma_\kappa = 1.0,\ \sigma_\epsilon = 1.31$ and the bed friction term c_f is defined as

$$c_f = g\frac{n^2}{h^{1/3}} = \frac{u_f^2}{|\mathbf{u}|} \tag{80}$$

and the strain rate tensor components are

$$S_{uu} = \left[\frac{\partial u}{\partial x}\right], \quad S_{uv} = \frac{1}{2}\left[\frac{\partial u}{\partial y} + \frac{\partial v}{\partial x}\right], \quad S_{vv} = \left[\frac{\partial v}{\partial y}\right] \tag{81}$$

The first order coupled formulation is applied according to the following algorithm:

$$\begin{aligned}
&\mathbf{U}_i^* = \mathbf{U}_i^n + \Delta t \sum_{k=1}^{NE} \mathbf{\Psi}_{k,i} \\
&\mathbf{U}_i^{**} = \mathbf{U}_i^* + \Delta t \mathbf{R}_{i,1}^* \\
&\mathbf{U}_i^{***} = \mathbf{U}_i^* + \Delta t \mathbf{R}_{i,2}^{**} \\
&\mathbf{U}_i^{n+1} = \mathbf{U}_i^{***} + \Delta t \mathbf{D}_i^{n+1}
\end{aligned} \tag{82}$$

where the term $\mathbf{R}_{i,1}$ is computed following the explicit formulation in (32) and the term $\mathbf{R}_{i,2}$ is computed using the implicit formulation in (33). A similar sequence is used for the second order coupled formulation. The estimation of the horizontal

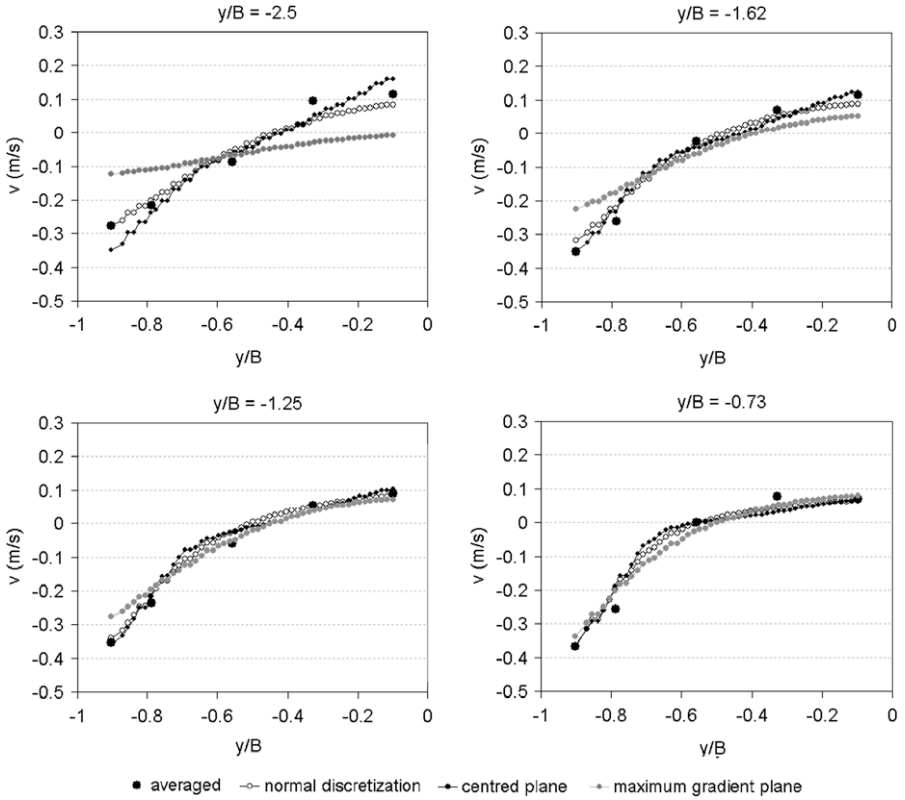

Fig. 26. Depth averaged measured velocity v and computed velocity in options 2, 5 and 6.

shear stress involves the computation of the gradient associated to the velocity components. This step is of primary importance when using turbulence models to evaluate correctly its effect in the smoothing of recirculating flows. In the case of triangular meshes the evaluation of the velocity gradients can be done by constructing interpolation planes from the information stored in the cell of interest and the information stored in the neighbouring cells [7]. One possibility is to use only the information stored in the surrounding cells, as in the LCD technique[1], defining the plane $j_1\widehat{j_2 j_3}$, that for sake of clarity will be called centred plane. In the context of interpolation techniques this option provides a small increment in the accuracy when moving to second order approach. For that reason it may seem necessary to move to more complex approximations. For instance, another possibility is to select the plane with maximum slope among the four planes that can be defined $i\widehat{j_2 j_3}$, $j_1\widehat{i j_3}$, $j_1\widehat{j_2 i}$ and $j_1\widehat{j_2 j_3}$ as in the MLG technique[1], that we will refer to as maximum gradient plane. Instead, a technique able to handle both rectangular and triangular meshes is proposed

$$
\begin{aligned}
S_{uv_i} &= \frac{1}{2}\left(\sum_{k=1}^{NE}\left(\frac{\delta u n_y}{d_{\mathbf{n}}}\right)\right)\left(\sum_{k=1}^{NE}|n_y|\right)^{-1} + \frac{1}{2}\left(\sum_{k=1}^{NE}\left(\frac{\delta v n_x}{d_{\mathbf{n}}}\right)\right)\left(\sum_{k=1}^{NE}|n_x|\right)^{-1} \\
S_{uu_i} &= \left(\sum_{k=1}^{NE}\left(\frac{\delta u n_x}{d_{\mathbf{n}}}\right)\right)\left(\sum_{k=1}^{NE}|n_x|\right)^{-1} \\
S_{vv_i} &= \left(\sum_{k=1}^{NE}\left(\frac{\delta v n_y}{d_{\mathbf{n}}}\right)\right)\left(\sum_{k=1}^{NE}|n_y|\right)^{-1}
\end{aligned}
\tag{83}
$$

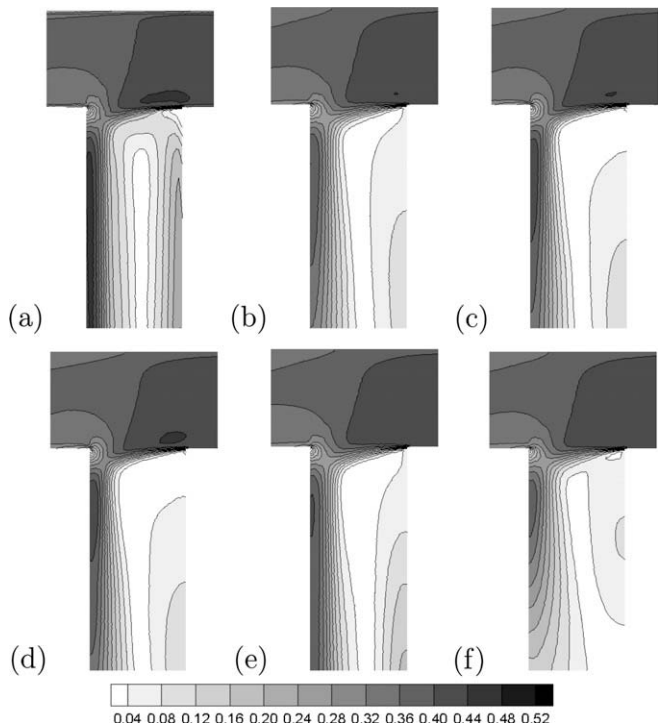

Fig. 27. Numerical results for the module of the velocity, in options 1–6 in (a)–(f), respectively.

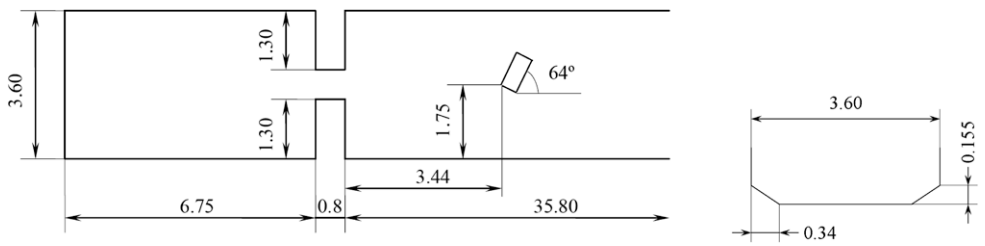

Fig. 28. Channel configuration and cross-section in the main channel. Dimensions in meters.

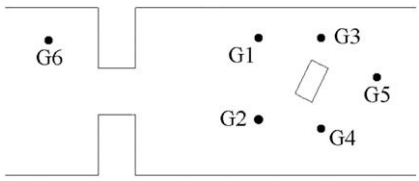

Fig. 29. Sketch of the location of the gauging points where the velocity was measured.

Table 6
Number of cells for the meshes in the dam-break flow case.

Structured	$M_{1,1}$	$M_{1,2}$	$M_{1,3}$	$M_{1,4}$	$M_{1,5}$
	12,212	50,262	107,336	505,262	1,011,396
Unstructured	$M_{2,1}$	$M_{2,2}$	$M_{2,3}$	$M_{2,4}$	$M_{2,5}$
	12,726	51,172	101,715	490,004	1,031,532

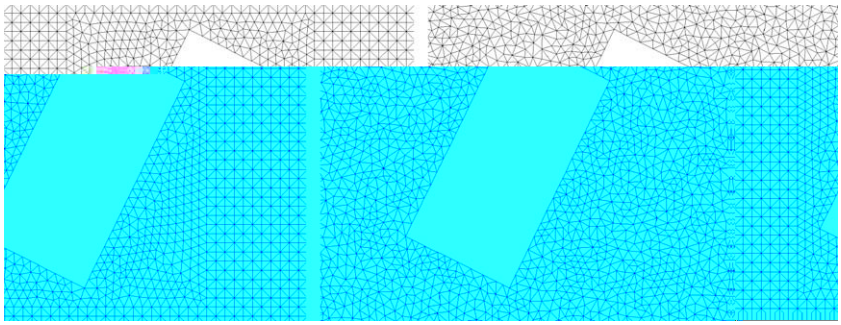

Fig. 30. Detail of meshes $M_{1,3}$ (right) and $M_{2,3}$ (left).

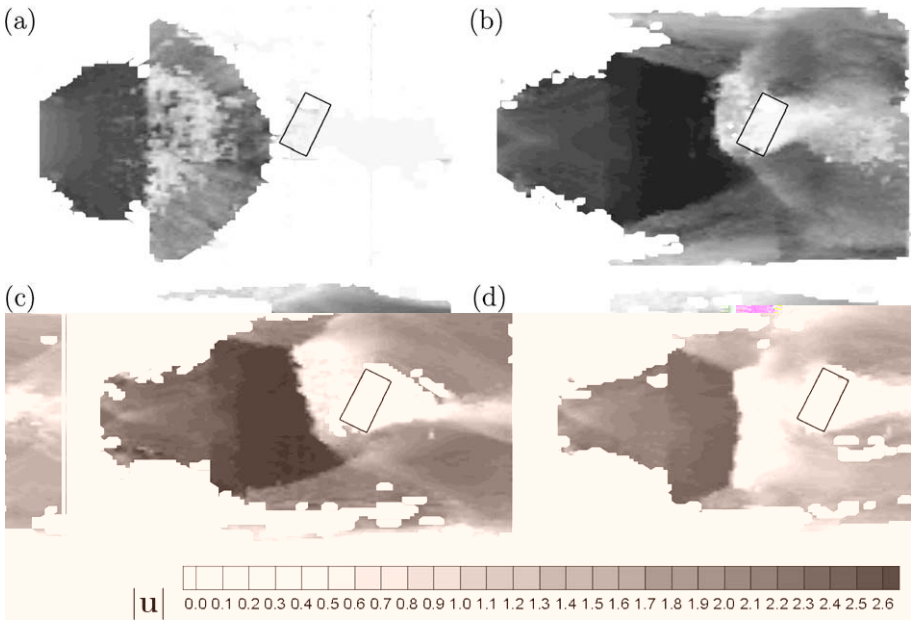

Fig. 31. Module of the surface velocity measured at $t = 1$ s (a), 3 s (b), 5 s (c) and 5 s (d).

that, in the case of structured quadrangular meshes, provides second order in space, often used in finite difference methods. This technique will be referred to as normal edge discretization.

4.3.1. 90° dividing flow in open channels

The simulations based on the turbulence model are tested using experimental data. The experiments, as described in [20], where performed in a 90° dividing flow horizontal channel with the dimensions indicated in Fig. 21(a). The main channel and the branch channel are 0.305 m high and 0.610 m wide. They are made of 12.7 mm Plexiglas plates and rest on a steel frame. The flow enters the main channel after passing through a transition that contains screens and honey combs. This ensures properly developed flow with low turbulence in the flume. At the end of the main and branch channels, control gates are placed to regulate the flow depth. The maximum discharge error was estimated to be 3%. A Laser Doppler Anemometry (LDA) unit was used to measure the mean velocity components of the flow fields. The error of the velocity was estimated to be 1%. The coordinate system used to record data is shown in Fig. 21(b). Measurements were always made only after steady state flow conditions were attained.

The selected experiments correspond to an inlet discharge $Q_u = 0.047\ \mathrm{m}^3/\mathrm{s}$ in the main channel. This is imposed as upstream boundary condition in the simulation while the water level surface $h = 0.184$ m is imposed downstream of the main channel and $Q_b = 0.07\ \mathrm{m}^3/\mathrm{s}$ downstream of the branch channel. The simulation was performed on an unstructured mesh with 47,395 cells using a Manning coefficient $n = 0.012\ \mathrm{s\,m}^{-1/3}$.

Table 5 summarizes the numerical options used in this case. In option 1 the numerical solution is computed using the plain shallow water equations. In the rest of the options the turbulence model in (82) is included. Options 2–4 are computed using the normal edge discretization, using first order in option 2, and using second order over the discharges and the discharges and the transported scalars in 3 and 4, respectively. Options 5 and 6 are computed using the first order approach with turbulence using the centred plane and maximum gradient plane techniques, respectively.

Fig. 22 is the plot of the velocity component u measured at different water depths ($z/B = 0.011,\ z/B = 0.033,\ z/B = 0.098,\ z/B = 0.164,\ z/B = 0.229$), the depth average of the measured u velocity and the computed depth averaged velocity using options 1 and 2 at different cross-sections. Fig. 23 is the corresponding plot for the velocity component v. These results indicate that the turbulence model produces velocities closer to the experimental depth average velocity than the plain shallow water model due to the smoothing effect in the recirculation areas.

Figs. 24 and 25 are the corresponding plots for the u and v components, respectively, using options 2 and 3. The velocities are only plotted in the secondary branch, as in the other options no appreciable differences are observed. These figures make clear that second order does not provide a benefit over first order as far as the velocities are concerned.

It is well known that the $\kappa-\epsilon$ method does not work well under some flow conditions [9]. When stagnation points appear, as in this case near the corner, the production of turbulent kinetic energy is over-predicted, given values of κ much larger than the measured ones. For options 2–4 the normal edge discretization technique generates enough dissipation, increasing the quality of the results. The centred plane technique provides similar levels of turbulence. On the other hand an excessive

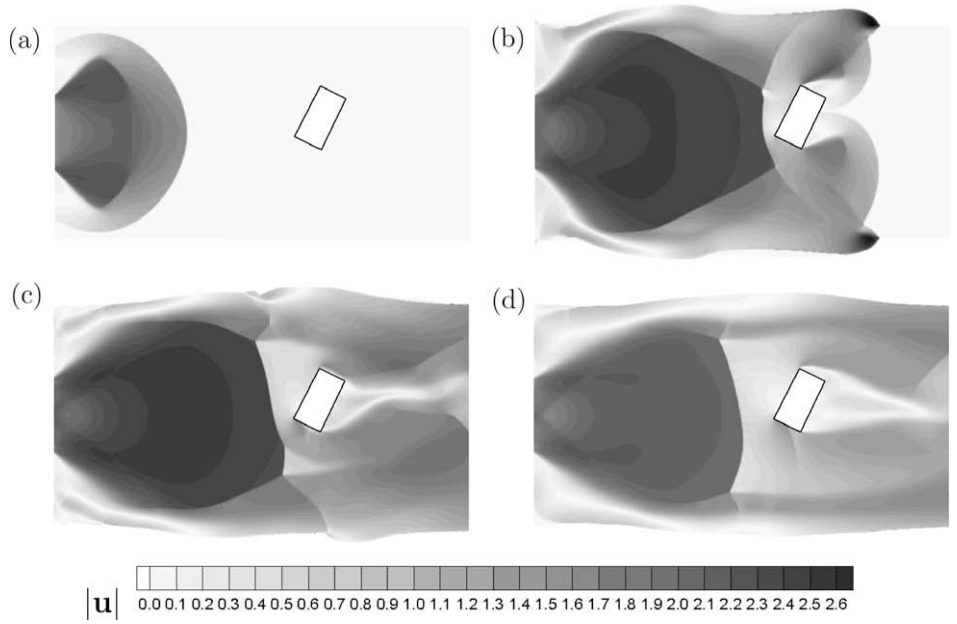

Fig. 32. Module of the depth averaged velocity computed using the $\kappa-\epsilon$ turbulence model at $t = 1$ s (a), 3 s (b), 5 s (c) and 15 s (d). Grid $M_{1.5}$.

amount of diffusion is included in the solution when using the maximum gradient plane technique, as Fig. 26 shows. This can lead to the wrong conclusion that the use of second order methods would be necessary to avoid the excessive diffusion of velocity maps.

Fig. 27 shows the contour plots for the module of the velocity for options from 1 to 6 in (a) to (f), respectively. The shape of the recirculation area calculated by any of the options 2–6 is much smoother than the solution from the shallow water model (option 1). However, no significant differences are introduced in the solutions by enforcing second order in the discharges or the transported scalars. The results from the uncoupled model are not shown because they are identical in this case of smooth water surface.

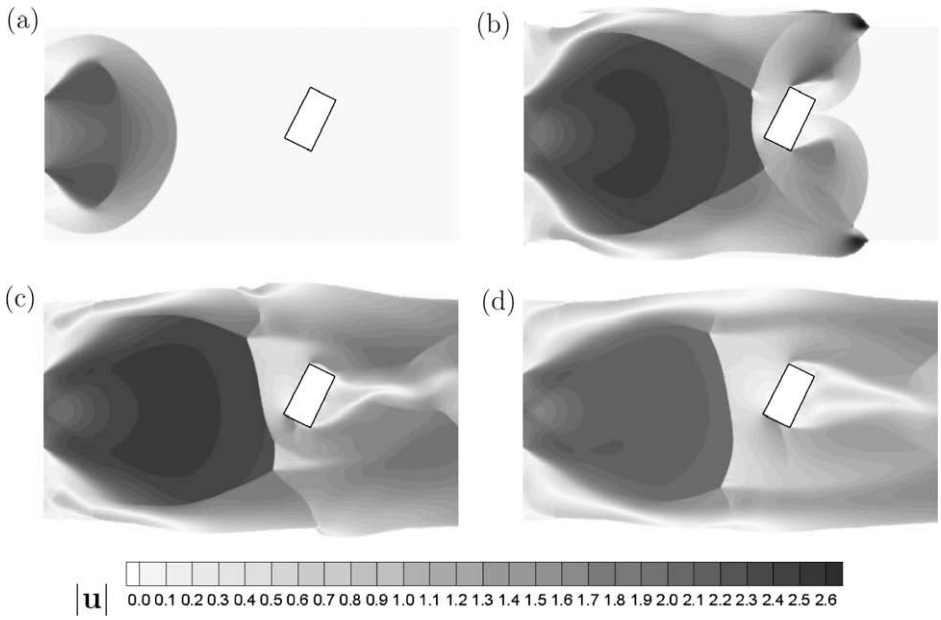

Fig. 33. Module of the depth averaged velocity computed using the $\kappa-\epsilon$ turbulence model at $t = 1$ s (a), 3 s (b), 5 s (c) and 15 s (d). Grid $M_{2.5}$.

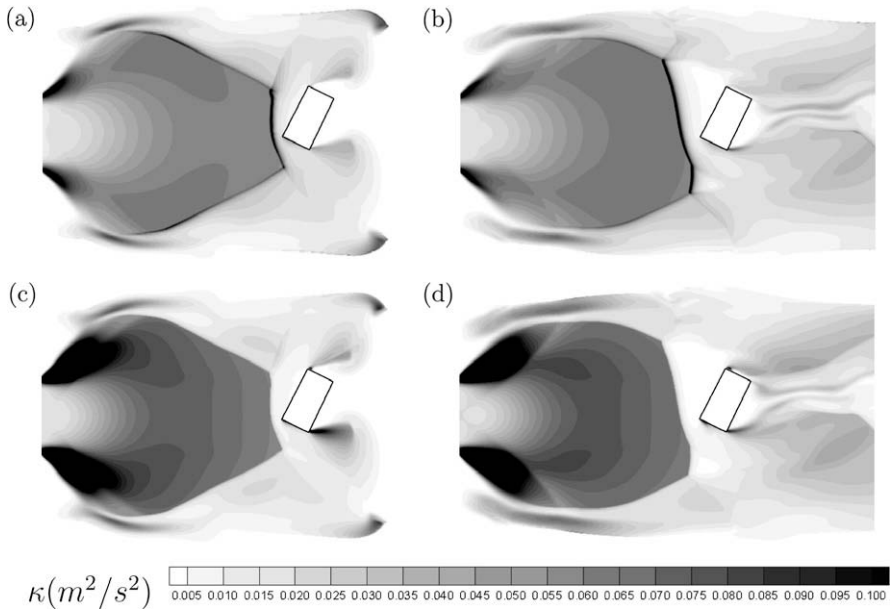

Fig. 34. Kinetic turbulent energy computed at $t = 3$ s (a) and (c) and $t = 5$ s (b) and (d) using the coupled formulation (a,b) and the uncoupled formulation (c,d). Grid $M_{1.5}$.

4.3.2. Dam-break flow against an isolated obstacle

In this numerical test case the flow around an obstacle induced by a dam-break is simulated. It has been chosen to study the behaviour of the solutions in presence of strong gradients in the conserved variables. The experiments were carried out in the Civil Engineering Laboratory of the Universit Catholique de Louvain (UCL) in Belgium [25]. The set-up consists of a reservoir connected to a symmetrical trapezoidal channel (the channel dimensions and shape are indicated in Fig. 28). A gate separates the reservoir from the channel where a rectangular obstacle 0.40 m wide and 0.80 m long is inserted. The channel has a nil slope and a Manning friction coefficient was estimated to $n = 0.010$ s m^1/3. Initial conditions for the experiment are a uniform water depth of 0.40 m in the reservoir and a uniform depth of 0.02 m in the channel. It is assumed that the downstream boundary does not influence the flow during the experiment. The time evolution of the velocity was measured using resistive gauges and Acoustic Doppler Velocimeters (ADV) at a height of 3.6 cm above the channel bed at several gauging stations. Their locations are shown in Fig. 29. Also, the surface velocity field in the area around the building was registered using digital imaging techniques. For more details see [25].

The numerical domain was discretized using two kinds of triangular grids, structured (M_1) and unstructured (M_2), of five different degree of refinement in order to analyze the sensitivity of the numerical results to these features. Table 6 contains the notation used to refer to all the grids used and the number of cells involved in every case. Fig. 30 shows a zoom view of the discretization of the area near the obstacle.

Fig. 31 are plots of the digital imaging measured surface velocity at $t = 1$, 3, 5 and 15 s. Fig. 32 are plots of the computed module of depth averaged velocity on the finest structured grid $M_{1,5}$ using the κ—ϵ turbulence model at $t = 1$ s (a), 3 s (b), 5 s (c) and 15 s (d). Fig. 33 are the equivalent plots on the finest unstructured grid $M_(2,5)$. All of them show a qualitative agreement between experimental and computational patterns.

Fig. 34 are plots of the kinetic turbulent energy computed at $t = 3$ s (a) and (c) and $t = 5$ s (b) and (d) using the coupled formulation (a,b) and the uncoupled formulation (c,d) on grid $M_{1,5}$. Fig. 35 shows again the kinetic turbulent energy computed with the coupled formulation at $t = 3$ s (a) and (c) and $t = 5$ s (b) and (d) using the two different grids $M_{1,5}$ (a,b) and $M_{2,5}$ (c,d). The coupled formulation provides a kinetic turbulent energy distribution coherent with the hydraulic jumps location whilst the uncoupled formulation leads to the generation of an excessive amount of kinetic turbulent energy in some regions. The influence of the kind of grid on the quality of the results is small but the particular discretization chosen (83) for the turbulent kinetic energy production terms is sensitive. As a consequence, the results on the structured grid show sharper profiles of this variable in the regions of strong velocity gradients.

Fig. 36 displays the comparisons of the measured u and v velocity components and the corresponding computed variables using the shallow water model on the structured grids. The plots represent time evolution of these variables at four gauge locations (probes G2–G5) and the numerical results from the five meshes are shown. The plots corresponding to probe G2 indicate that the shock location is sensitive to the grid refinement chosen. The behaviour of the solutions at probes G3 and G4 is rather indifferent to the grid refinement. The velocities at probe G5, located at the wake of the obstacle, follow an oscillatory time evolution. The numerical solutions obtained at this point are very sensitive to the grid refinement. In general, all the grids used predict oscillatory velocities of different amplitude, being the results from the finest grid the closest to the experimental data.

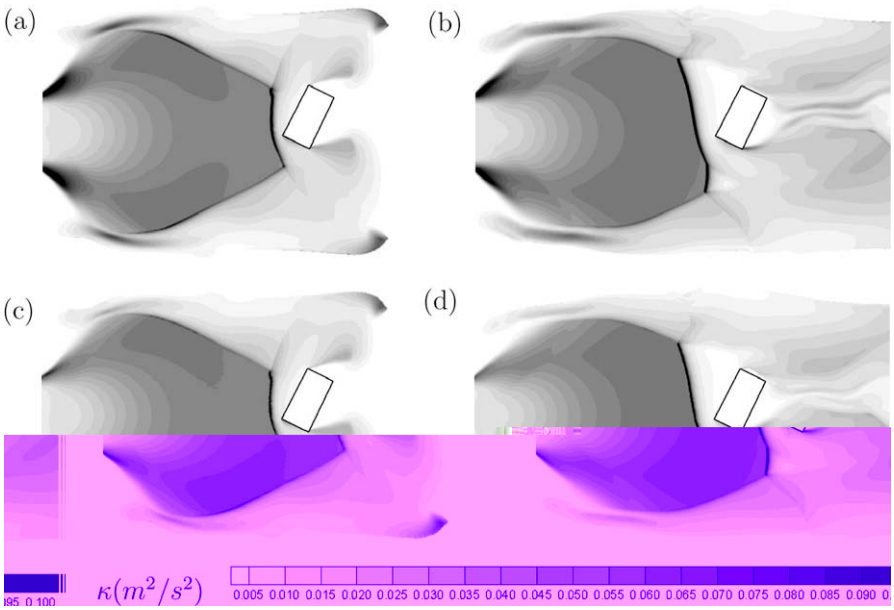

Fig. 35. Kinetic turbulent energy computed with the coupled formulation at $t = 3$ s (a) and (c) and $t = 5$ s (b) and (d) using $M_{1,5}$ (a,b) and $M_{2,5}$ (c,d).

Fig. 37 displays the comparisons of the measured u and v velocity components and the corresponding computed variables using the κ–ϵ shallow water model on the structured grids. The plots represent the time evolution at the same gauge locations (probes G2–G5) and the numerical results from the five meshes are shown. The plots corresponding to probe G2 indicate that the shock location tends to be better predicted with most of the grids used. The behaviour of the solutions at probes

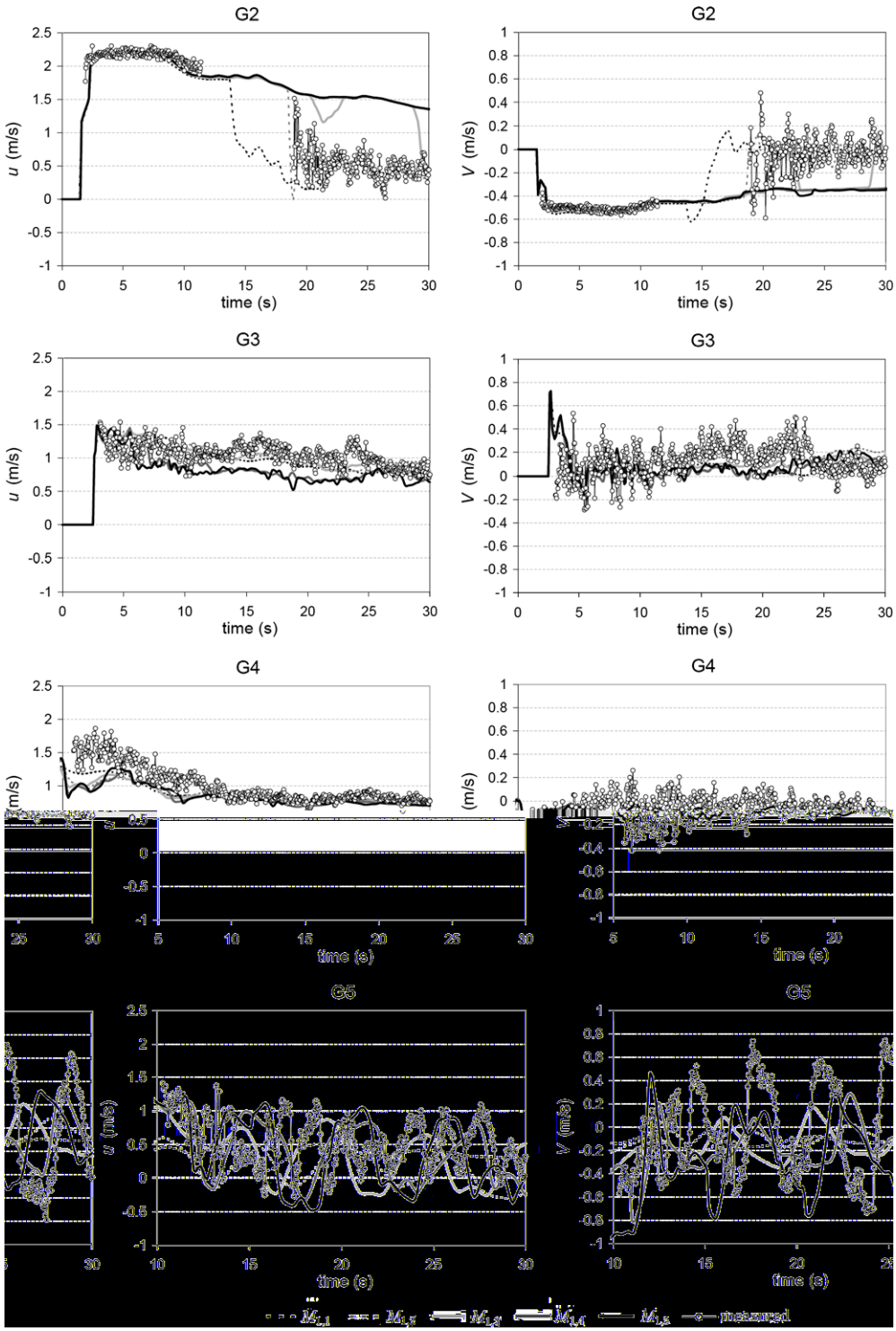

Fig. 36. Measured u and v velocities and shallow water computed velocities.

G3 and G4 is almost identical to the results with the plain shallow water model. The oscillations predicted for the velocities at probe G5 are now smoothed with damped extremes.

Fig. 38 displays the comparisons of the measured u and v velocity components and the corresponding computed variables using the shallow water model on the unstructured grids of different number of cells. The plots corresponding to probes G2–G4 are almost identical to those obtained on the other type of mesh except for the coarsest grid. The numerical velocities at

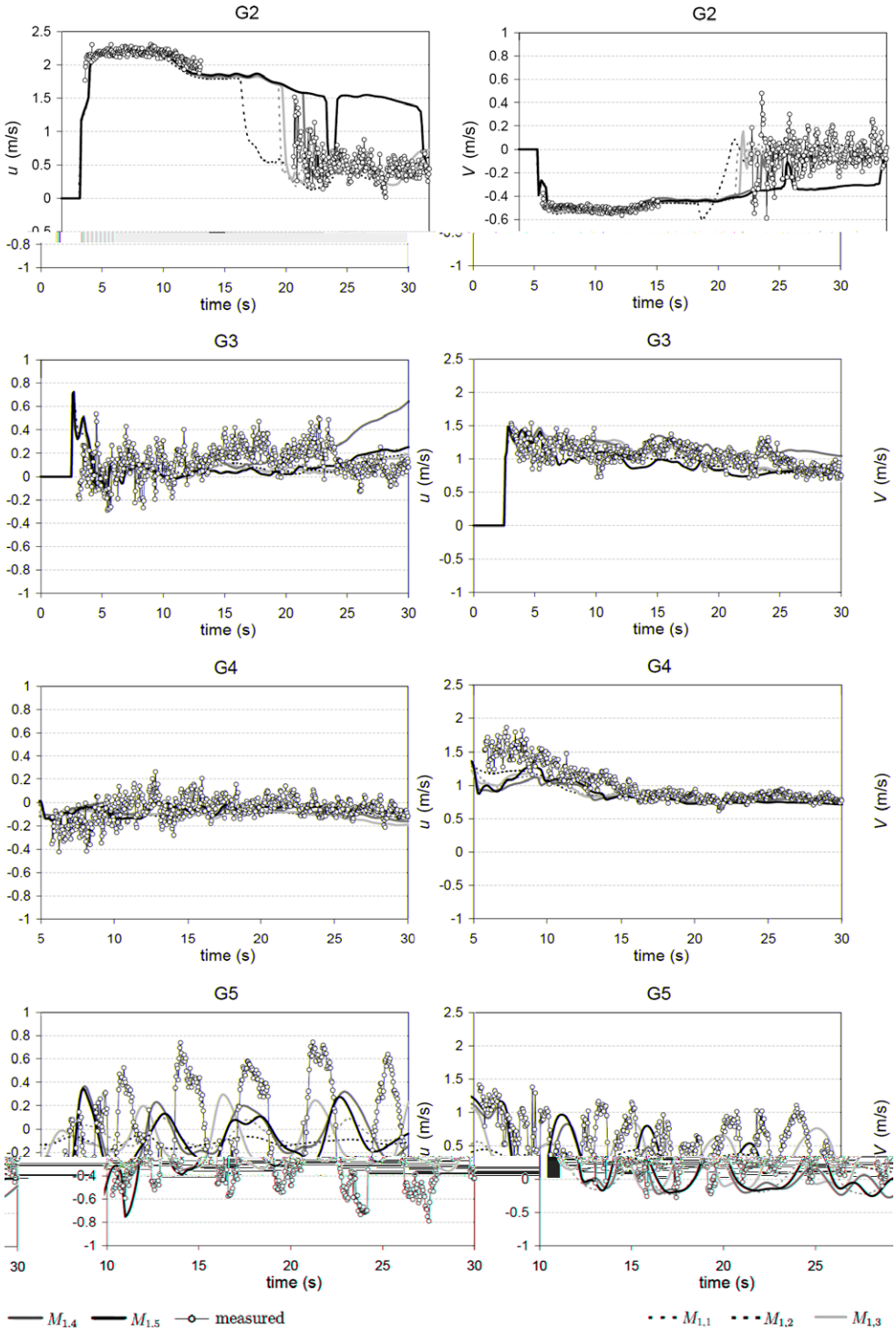

Fig. 37. Measured u and v velocities and $\kappa-\epsilon$ shallow water computed velocities.

probe G5, follow an oscillatory pattern again and display a high sensitivity to the grid refinement. The detailed time evolution of the velocities at this location is different from the evolution predicted by the computation on the structured grids.

Fig. 39 displays the comparisons of the measured u and v velocity components and the corresponding computed variables using the κ—ϵ shallow water model on the unstructured grids. The most noticeable feature is that the time evolution of the

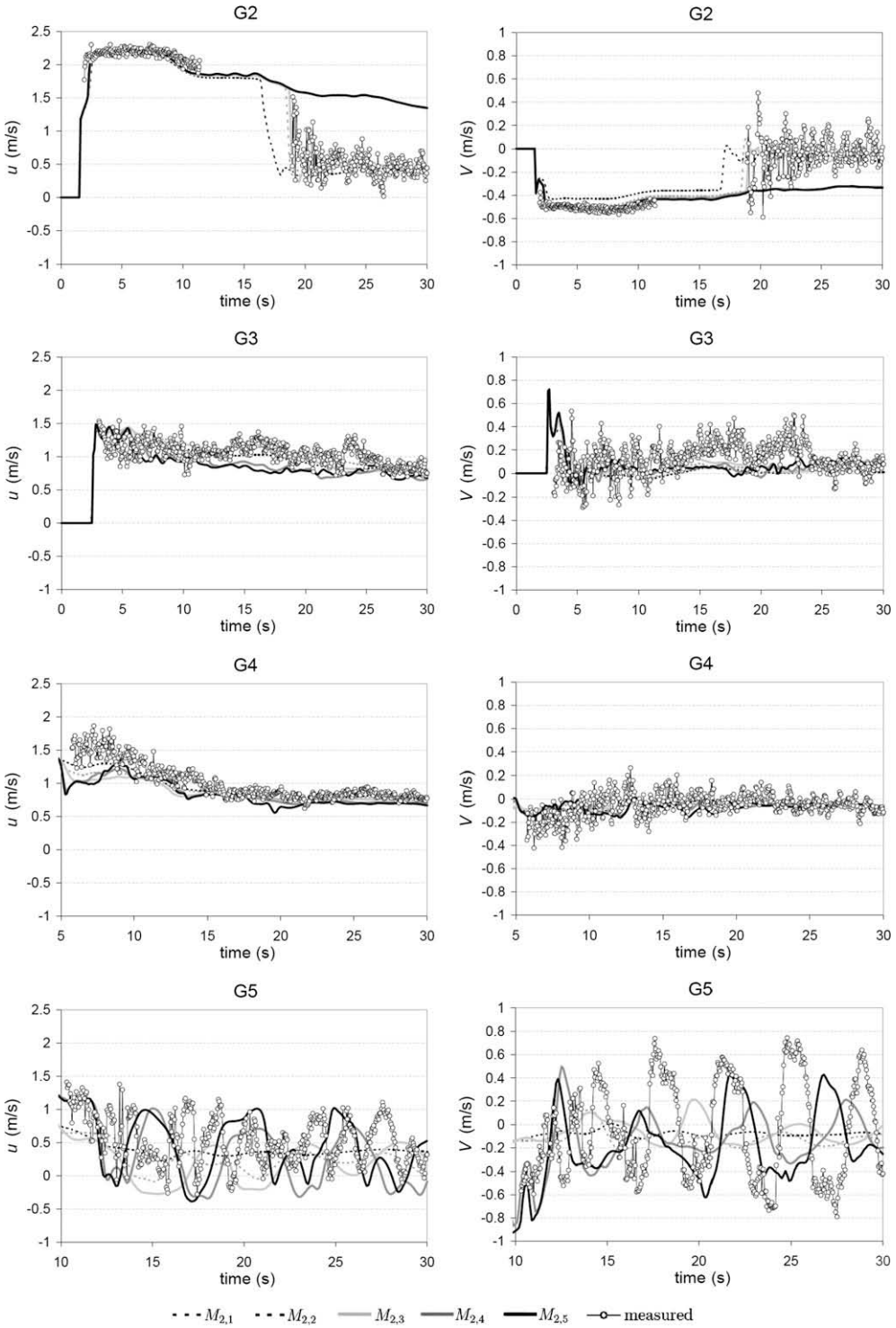

Fig. 38. Measured u and v velocities and shallow water computed velocities.

velocities at probe G5 is now very similar to the tendency predicted by the computation on the structured grids. This can be interpreted by the damping effect of the turbulent viscosity introduced by the model that is of the same order in both types of grid.

In general, there is not a good agreement between experimental data and numerical results even with the finest mesh. A good mean behaviour for gauge locations 3 and 4 can be observed from all the approaches. The location G5 is the zone of

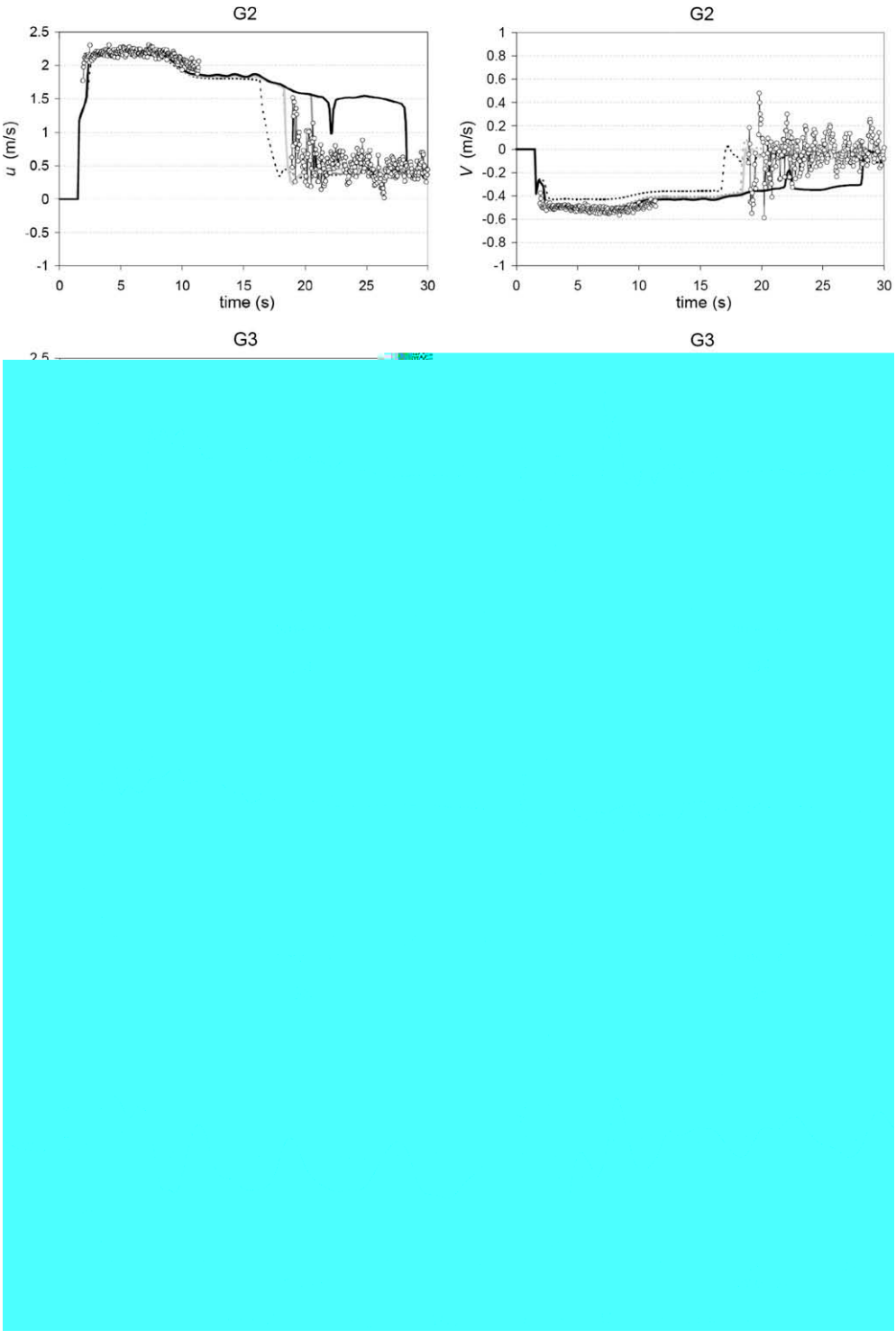

Fig. 39. Measured u and v velocities and $\kappa-\epsilon$ shallow water computed velocities.

high turbulence and the $\kappa-\epsilon$ shallow water model does not help to enhance the quality of the results over the plain shallow water solution.

5. Conclusions

The extension of a finite volume model, suitable for unsteady shallow water over dry irregular beds and able to preserve the C-property with non-zero velocity steady states, to more general problems involving multi-component transport has been presented and several numerical options have been proposed. The method is designed to work either on structured or unstructured triangular grids. The model, under different computational options, has been validated using test cases with analytical solutions as well as laboratory measurements in order to evaluate their relative performance. The main conclusions that can be drawn from these are:

- In absence of diffusion and reaction, the multi-component advection by an unsteady flow over variable bed requires a coupled formulation of the mass and momentum flow dynamics and mass of the transported components in order to achieve a conservative tracking of the solute fronts. Uncoupled resolution of the system leads to non-conservative, incorrect results.
- In this context, the coupled formulation is not sufficient to preserve monotone solutions in the primitive concentration variables. This can only be achieved by means of a systematic control on the updating quantities.
- The technique for conservative flux redistribution to overcome the time step size restrictions induced by the source terms of the conservation laws can be successfully used in multi-component transport. The results obtained are identical to those that could be obtained at a higher computational cost.
- In cases of multi-component transport with reaction terms, the uncoupled formulation is only valid when there are not gradients in the water depth variable. Otherwise, the numerical error introduced by this formulation can be misinterpreted as an excessive numerical smearing.
- When solving a complex dynamic problem involving scalar transport, production and extinction such as a depth averaged $\kappa-\epsilon$ turbulence model, the numerical approximation used may be of utmost importance. For steady flow with uniform or nearly uniform surface level, both coupled and uncoupled formulations provide similar results and both first and second order methods furnish similar degree of accuracy. For unsteady flow with rapidly varying water surface levels, the uncoupled formulation does not provide correct results. The consequences of being careless in the choice of the numerical technique can be misleading and obscure the actual necessity of using the turbulence model. The coupled formulation of the $\kappa-\epsilon$ shallow water model has proved less sensitive to the type of grid used than the plain shallow water model for the prediction of the velocities.

References

[1] P. Batten, C. Lambert, D.M. Causon, Positively conservative high-resolution convection schemes for unstructured elements, Int. J. Numer. Method Eng. 39 (1996) 821–1838.
[2] L. Begnudelli, F. Sanders, Unstructured grid finite-volume algorithm for shallow-water flow and scalar transport with wetting and drying, J. Hydraul. Eng. 132 (2006) 371–384.
[3] F. Benkhaldoun, I. Elmahi, M. Sea, Well-balanced finite volume schemes for pollutant transport by shallow water equations on unstructured meshes, J. Comput. Phys. 226 (2007) 180–203.
[4] P. Brufau, M.E. Vázquez-Cendón, P. García-Navarro, A numerical model for the flooding and drying of irregular domains, J. Numer. Method Fluid 39 (2002) 247–275.
[5] J. Burguete, P. García-Navarro, Efficient construction of high-resolution TVD conservative schemes for equations with source terms: application to shallow water flows, Int. J. Numer. Method Fluid 37 (2001) 209–248.
[6] J. Burguete, P. García-Navarro, J. Murillo, Preserving bounded and conservative solutions of transport in one-dimensional shallow-water flow with upwind numerical schemes: application to fertigation and solute transport in rivers, Int. J. Numer. Method Fluid 56 (2008) 1731–1764.
[7] L. Cea, L. Pena, J. Puertas, M.E. Vázquez-Cendón, E. Pea, Application of several depth-averaged turbulence models to simulate flow in vertical slot fishways, J. Hydraul. Eng., ASCE 39 (2007) 133–160.
[8] R. Courant, E. Isaacson, M. Rees, On the solution of nonlinear hyperbolic differential equations by finite differences, Commun. Pure Appl. Math. 5 (1952) 243–255.
[9] P. Durbin, On the κ–ϵ stagnation point anomaly, Int. J. Heat Fluid Flow 17 (1996) 89–90.
[10] J. Fe, F. Navarrina, J. Puertas, P. Vellando, D. Ruiz, Experimental validation of two depth-averaged turbulence models, J. Numer. Method Fluid (2008), doi:10.1002/fld.1880.
[11] E. Godlewsky, P.A. Raviart, Numerical Approximation of Hyperbolic Systems of Conservation Laws, vol. 403, Springer-Verlag, New York, 1996.
[12] J.B. Goodman, R.J. LeVeque, On the accuracy of stable schemes for 2D scalar conservation laws, Math. Comput. 45 (1985) 15–21.
[13] M.E. Hubbard, P. García-Navarro, Flux difference splitting and the balancing of source terms and flux gradients, J. Comput. Phys. 165 (2000) 89–125.
[14] R.J. Leveque, Finite Volume Methods for Hyperbolic Problems, Cambridge University Press, New York, 2002. p. 380.
[15] J. Murillo, J. Burguete, P. Brufau, P. García-Navarro, Coupling between shallow water and solute flow equations: analysis and management of source terms in 2D, Int. J. Numer. Method Fluid 49 (2005) 267–299.
[16] J. Murillo, P. García-Navarro, J. Burguete, P. Brufau, A conservative 2D model of inundation flow with solute transport over dry bed, Int. J. Numer. Method Fluid 52 (2006) 1059–1092.
[17] J. Murillo, P. García-Navarro, J. Burguete, P. Brufau, The influence of source terms on stability accuracy and conservation in two-dimensional shallow flow simulation using triangular finite volumes, Int. J. Numer. Method Fluid 54 (2007) 543–590.
[18] J. Murillo, J. Burguete, P. García-Navarro, Analysis of a second-order upwind method for the simulation of solute transport in 2D shallow water flow, Int. J. Numer. Method Fluid 56 (2008) 661–686.
[19] J. Murillo, P. García-Navarro, J. Burguete, Time step restrictions for well-balanced shallow water solutions in non-zero velocity steady states, Int. J. Numer. Method Fluid (2009), doi:10.1002/fld.1939.

[20] J. Qu, Three-dimensional turbulence modelling for free surface flows. Ph.D. Thesis, Concordia University, Montreal, Canada, 2005.
[21] A.K. Rastogi, W. Rodi, Predictions of heat and mass transfer in open channels, J. Hydraul. Div., ASCE (1978) 397–420.
[22] P.L. Roe, A basis for upwind differencing of the two-dimensional unsteady Euler equations, Numerical Methods in Fluid Dynamics, vol. II, Oxford University Press, Oxford, 1986.
[23] G. Rosatti, J. Murillo, L. Fraccarollo, Generalized Roe schemes for 1D two-phase free-surface flows over a mobile bed, J. Comput. Phys. 54 (2007) 543–590.
[24] J.C. Rutherford, River Mixing, Wiley, New York, 1994. p. 21.
[25] S. Soares-Frazao, Y. Zech, Experimental study of dam-break flow against an isolated obstacle, J. Hydraul. Res. 45 (1994) 27–36.
[26] W.C. Thacker, Some exact solutions to the nonlinear shallow water equations, J. Fluid Mech. 107 (1981) 499–508.
[27] E.F. Toro, Riemann Solvers and Numerical Methods for Fluid Dynamics, Springer, Berlin, 1997. p. 526.
[28] E.F. Toro, Shock-Capturing Methods for Free-Surface Shallow Flows, Wiley, New York, 2001. p. 109.
[29] M.E. Vázquez-Cendón, Improved treatment of source terms in upwind schemes for the shallow water equations in channels with irregular geometry, J. Comput. Phys. 148 (1999) 497–498.
[30] M.E. Vázquez-Cendón, Implicit and explicit upwind schemes for the 2D shallow water equations in unstructured meshes, Numer. Model. Hydrodynam. Syst., Zaragoza 1 (1999) 251–321.
[31] M. Wierse, A new theoretically motivated higher order upwind scheme on unstructured grids of simplices, Adv. Comput. Math. 7 (1997) 303–335.